CHALMERS
UNIVERSITY OF TECHNOLOGY

Investigation of membrane fouling layer characteristics using fluid dynamic gauging

Influence of surface charge

Master's thesis in Innovative and Sustainable Chemical Engineering

HILDA SANDSTRÖM

Department of Chemistry and Chemical Engineering
CHALMERS UNIVERSITY OF TECHNOLOGY
Gothenburg, Sweden 2018

Investigation of membrane fouling layer characteristics using fluid dynamic gauging

Influence of surface charge

Master's thesis in Innovative and Sustainable Chemical Engineering

Hilda Sandström

Forest Products and Chemical Engineering
Department of Chemistry and Chemical Engineering
CALMERS UNIVERISTY OF TECHNOLOGY
Gothenburg, Sweden 2018

Investigation of membrane fouling layer characteristics using fluid dynamic gauging

Influence of surface charge

HILDA SANDSTRÖM

SUPERVISORS:
Dr. Mi Zhou
Ass. Prof. Tuve Mattsson

EXAMINER:
Prof. Hans Theliander

Forest Products and Chemical Engineering
Department of Chemistry and Chemical Engineering
CALMERS UNIVERISTY OF TECHNOLOGY
Gothenburg, Sweden 2018

Investigation of membrane fouling layer characteristics using fluid dynamic gauging
Influence of surface charge

HILDA SANDSTRÖM
Forest Products and Chemical Engineering
Department of Chemistry and Chemical Engineering
Chalmers University of Technology

Abstract

Separation processes are often very energy demanding and it is crucial to develop more energy efficient methods. Membrane separation is a method, with a potentially very low energy demand, where solid particles or dissolved species are separated by a selective membrane. Membrane separations are today used in a range of applications and are expected to become an important operation in biorefineries that are under development.

Membrane fouling decreases the capacity of the membrane operation and challenges stable operation of membrane separations. To improve the capacity of membrane operations, more knowledge about the mechanisms in fouling are needed. There are some different techniques to characterise fouling, and for example measure the fouling build-up on membranes. Fluid dynamic gauging is such a technique, which can be used to measure the thickness and cohesive strength of the fouling layer.

In this study, fluid dynamic gauging is used to investigate the fouling layer thickness and cohesive strength in membrane cross-flow filtration of microcrystalline cellulose. The fouling behaviour is compared at two pH levels for two different membranes, regenerated cellulose membrane and polyethersulfone membrane. It is found that a suspension of low pH (2.9), where the surface charge of the particles is close to zero, results in thicker and stronger fouling layers, with a relatively slow flux decline. While for unadjusted pH, where the particles are negatively charged, the fouling layers are thinner and less resistant to shear stress, and flux decreases to a low level faster than for the other case. The difference in fouling between the two levels of pH, is most likely due to differences in the fouling mechanisms, where the pore openings of the membrane are blocked at unadjusted pH. There were no noticeable differences between the two membranes, even though they are made of different materials.

Key words: Fluid dynamic gauging, cross-flow filtration, microcrystalline cellulose, electrostatic interactions

Acknowledgements

The completion of this master's thesis was made possible with the contribution from several people, whom I would like to acknowledge. I would like to start by expressing my appreciation to my examiner, Hans Theliander, for the opportunity of writing this master's thesis. My supervisor, Tuve Mattsson, for the possibility of doing this study and for all the help and encouragements. My supervisor, Mi Zhou, for all the supervision and help, both during experimental work together and in the analysing of the results. I would also like to thank Tor Sewring, for helping me with FBRM measurements, and Anders Ahlbom for assisting me in experimental work when needed.

Finally, I would like to thank everybody at the division of Forest Products and Chemical Engineering, for all the support and interest in my master's thesis and for giving me a great work environment during these weeks.

Hilda Sandström,
September 2018

Table of Contents

1 Introduction

Separation operations are very energy demanding parts in chemical industry, therefore it is crucial to develop more energy efficient separation techniques. Pressure driven separation processes are often more energy efficient than those driven by thermal energy, such as distillation, and hence offers a good option for efficient separations. One such separation technology is membrane separation, which uses a selective barrier, the membrane, to separate solid particles or dissolved species. The selectivity of the membrane is mainly based on size of the species, but their electrostatic properties may also play a role. Membrane separations are widely used in production of potable water from seawater e.g. (Aboabboud and Elmasallati, 2007), in cleaning of process effluents e.g. (Bruggen et al., 2003) and to separate macromolecules in food and drug industries e.g. (Ahmad and Ahmed, 2014). It is also expected to become an important operation in biorefineries, for the concentrating, purification and fractionation of biomaterials.

A limitation of the efficiency in membrane filtration is fouling of the membrane, which is build-up of material on the membrane surface or in the pores of the membrane. This results in elevated transmembrane pressure or decreased permeate flux, which can severely jeopardise the membrane performance and increase the energy demand.

Traditionally, membrane fouling is described by the membrane flux decline, and it has been shown that fouling depends on the filtrated material, the operating conditions as well as the selected membrane. However, membrane studies have often been mainly focused on the flux decline, thus providing limited understanding to the characteristics of the fouling layers. Acquiring the properties of the fouling layers is crucial in minimizing or suppressing the growth of fouling layers and thus ameliorate the use of membranes. To achieve this, better measurement methods are needed.

One suggested technique to investigate the fouling characteristics is fluid dynamic gauging. It was first developed by Tuladhar et al. (2000), for measurements of the thickness of soft deposits on a surface. Later it has also been used to measure the strength of the deposits, which make it a good technique for the characterisation of membrane fouling (Chew et al., 2004a). Measuring the thickness and strength of the fouling layer would give better knowledge about its properties, which is crucial in optimizing membrane operations.

1.1 Aim

The aim of this study is to characterise the membrane surface fouling during the dewatering of microcrystalline cellulose by cross-flow microfiltration. The focus will be to investigate the effect of electrostatic interactions on foulant - foulant and foulant - membrane interactions and the properties of the formed fouling layers. The surface charge of the microcrystalline cellulose will be changed by altering the pH of the suspension.

1.2 Outline

In Chapter 2, a theoretical background to this study is given, the basic principles in membrane separations, how the performance of this technique depends on various conditions and some background on the modelling of membrane separations are given. The background of fluid dynamic gauging will also be introduced along with the applications for this technique. The material used in the experiments is also briefly presented.

The method and equipment used in this study are presented in Chapter 3, with descriptions of the experimental setup as well as conditions and procedure for performing the experiments. The results are reported in Chapter 4, along with discussions on the outcome of the measurements. Some general

conclusions are presented in Chapter 5 and the final chapter, Chapter 6, presents some suggestions for future work within the area.

1.3 Delimitations

- Filtration experiments were performed with microcrystalline cellulose, and no other foulant material was tested.
- The equipment for filtration and measurements limits the pressure span and concentrations in which filtration experiments can be conducted.
- Two pH levels are investigated in the study, one at which the microcrystalline cellulose is negatively charged and one at which the surface charge is close to zero.
- Two membranes are used in the investigation, one is a regenerated cellulose membrane and the other one is made of polyethersulfone.

2 Theoretical background

In this section, a theoretical background to the study is given. Including the basics in membrane filtration and membrane fouling, a short introduction of some methods to characterise fouling and a more thorough review of fluid dynamic gauging, finally the model material used in this study, microcrystalline cellulose, is introduced.

2.1 Membrane filtration

In membrane filtration, the membrane functions as a barrier, through which one of the species can pass more easily (Henley et al., 2011). The separation is pressure driven, which often results in energy efficient operations. There are two main modes of operation, dead-end filtration and cross-flow filtration. The two principles are illustrated in Fig. 1. In dead-end filtration, all the material will be deposited on the membrane surface or in the pores of the membrane, and the stream that passes through the membrane is called filtrate. In cross-flow filtration, the flow is parallel to the membrane surface, which introduces a fluid shear. This implies that only parts of the material will be deposited on the membrane and some of it also will be resuspended due to the shear stress, allowing longer operation times between cleaning (Lewis et al., 2017). The particles in the bulk flow will leave with the retentate at higher concentration. The viscosity of the retentate need to be low enough for the stream to flow past the membrane, this implies that a lower degree of dryness can be achieved in cross-flow filtration than in dead-end filtration. The liquid that passes through the membrane is called permeate and the average velocity of the bulk flow (feed and retentate) is called cross-flow velocity (CFV) (Mulder et al., 1991). Cross-flow filtration is treated in this study.

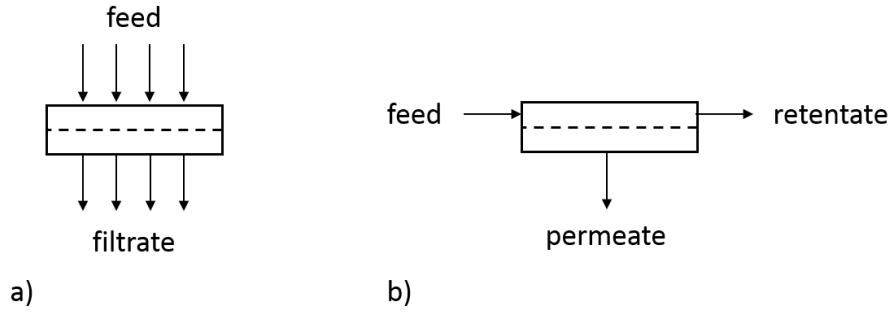

Figure 1. a) Dead-end filtration schematic, b) cross-flow filtration schematic.

Filtration can be performed either with constant pressure over the membrane, with constant flux through the membrane or with variation of both pressure and flux. In industry it is often important to keep a constant production, which make constant flux operation the most common.

2.1.1 Membranes

The usage areas for membranes are various, and therefore there is a large variety in the membrane properties. Membranes can be produced from either biological or synthetic raw material, with the latter being most widely used in industry. Synthetic membranes can be classified into four groups, depending on structural differences: porous membranes, homogeneous solid membranes, solid membranes carrying electrical charges and liquid or solid films. Moreover, the structure can be either symmetric or asymmetric. In symmetric membranes, the structure is identical in the whole membrane, and the flux depends on the thickness and transport resistance of the membrane. In asymmetric membranes, a thin film is the actual selective barrier, and the remaining material has a much lower flux resistance.

Furthermore, synthetic membranes can be constructed in many different materials, such as polymers, ceramics, glass, metals or liquids, to accommodate different applications (Strathmann, 2011a). In microfiltration, the most common materials are polymeric and ceramic, and the polymeric membranes are divided in two groups: hydrophilic and hydrophobic membranes (Mulder et al., 1991). The ceramic membranes are more chemically and thermally stable, while the polymeric membrane change properties and finally degrade with increased temperature. On the other hand, polymeric membranes are often less expensive to produce.

For industrial applications, the membranes are usually shaped and fixed into modules to fit the actual process. Usually the active membrane layer is supported by a porous material, to make it more resistant to pressure differences. The support structure is made in a suitable material such as fiberglass or perforated metal. Other types of support structure are hollow fibers, which are produced by spinning of a synthetic polymer, and monoliths with the membrane layer inside small channels of the material (Henley et al., 2011). If the membrane and support structures are flat, it can either be placed in plate-and-frame modules or rolled into spirals. The support material can also be tubular with the membrane surface facing either towards the outside or the inside of the tubes, giving modules where the permeate pass through the walls of the tubes and the retentate flows inside the tubes.

An important property of the membrane is the permselectivity, which describes the transport rate of different species through the membrane. This rate depends on the structure of the membrane, the size of the permeating component, the chemical properties and electrical charge of the membrane and permeating component, as well as the driving forces, due to gradients in concentration, pressure and electrical potentials.

For dilute aqueous mixtures, the selectivity of the membrane is often expressed as the retention (R). A solute or particle is partly or entirely retained by the membrane, and R describes the degree of retention of the specific component, Eq. 1.

$$R = 1 - \frac{c_p}{c_b} \tag{1}$$

Where c_p is the concentration of the solute or particle in the permeate, and c_b is the concentration in the feed bulk. If the retention equals to one, the component is entirely retained by the membrane and if the retention equals zero the membrane does not hinder the component (Strathmann, 2011a).

2.1.2 Membrane operations

Depending on the size of the filtered particles or dissolved species, membrane separations can be divided into different types. If the pore size is larger than approximately 0.1 µm, they are classified by the largest pore size of the membrane, and for smaller scales molecular weight cut-off (MWCO) is used for classification. MWCO is defined as the mass of a molecule that has a retention of more than 90% in the membrane. Microfiltration (MF) is usually specified by pore size, and is used for separation of suspended particles. The next level is ultrafiltration (UF), which is used to separate macromolecules. Following is nanofiltration (NF) and reverse osmosis (RO). NF is typically used for the separation of divalent salts and dissociated acids, and RO can separate monovalent salt and undissociated acids (Green et al., 2008). In Tab. 1, different membrane operations are presented along with their operating pressures, pore size and MWCOs. Some other types of membrane operations are pervaporation, with vaporisation through permselective membranes, and electrodialysis, with an electrical field as driving force (Berk, 2013). In this study, microfiltration is treated.

Table 1. Presentation of different membrane separation operations and the classification depending on operating pressure, pore size and molecular weight cut off (Berk, 2013) (Cardew and Le, 1998).

Filtration operation	Operating pressure (bar)	Pore size (µm)	Molecular weight cut off (Da)
Microfiltration (MF)	< 2	0.1-10	-
Ultrafiltration (UF)	2-10	0.001-0.1	10^2-10^6
Nanofiltration (NF)	10-40	0.0005-0.005	10^2-10^3
Reverse osmosis (RO)	30-100	-	10^1-10^2

The required operating pressure increases with decreasing sizes of the separated species, since the pore size is smaller and the osmotic pressure becomes more important for smaller species. In cross-flow filtration, the pressure difference over the membrane is reported as the transmembrane pressure (TMP). The pressure on the permeate side (P_{perm}) is normally constant both over time and along the membrane, but the pressure in the feed stream (P_{feed}) is usually higher than that in the retentate stream (P_{ret}), especially for high CFV or long membranes where the pressure drop due to friction becomes significant. The average value of the TMP can be obtained from Eq. 2. If the difference between P_{feed} and P_{ret} is negligible, it is enough to only use one value (Thuvander et al., 2014).

$$TMP_{avg} = \frac{P_{feed} + P_{ret}}{2} - P_{perm} \tag{2}$$

2.1.3 Flow through membranes

Darcy (1856) developed a model for flow through porous media, where he showed that the flow rate is related to the pressure drop. In Eq. 3, the Darcy equation for membrane separation is expressed as flux through the membrane.

$$J = \frac{1}{A_m}\frac{dV}{dt} = \frac{K_m}{\delta_m}\frac{TMP}{\mu} \tag{3}$$

Where J is the permeate flux, A_m the membrane area, V is the volume of permeate, t is time, K_m is the permeability of the membrane, δ_m is the thickness of the membrane and μ is the viscosity of the fluid. The original model did not take the viscosity of the fluid into consideration, but that have been added later. From the permeability of the membrane and membrane thickness, the membrane resistance (R_m) which will always be present, can be calculated as in Eq. 4.

$$R_m = \frac{\delta_m}{K_m} \tag{4}$$

Throughout the filtration process, the concentration of the solute or particle at the membrane surface (c_m) will become higher than the bulk concentration (c_b) due to the transport of bulk liquid towards the membrane and the retention of solute by the membrane, illustrated in Fig. 2. This will generate a concentration gradient between the membrane surface and the bulk liquid, which may lead to back-transport of solute by diffusion from the membrane surface. This gradient is called concentration

polarization, which leads to an additional resistance to filtration (R_{cp}). In microfiltration the particles are relatively large, and the back-diffusion will be relatively slow (Strathmann, 2011b).

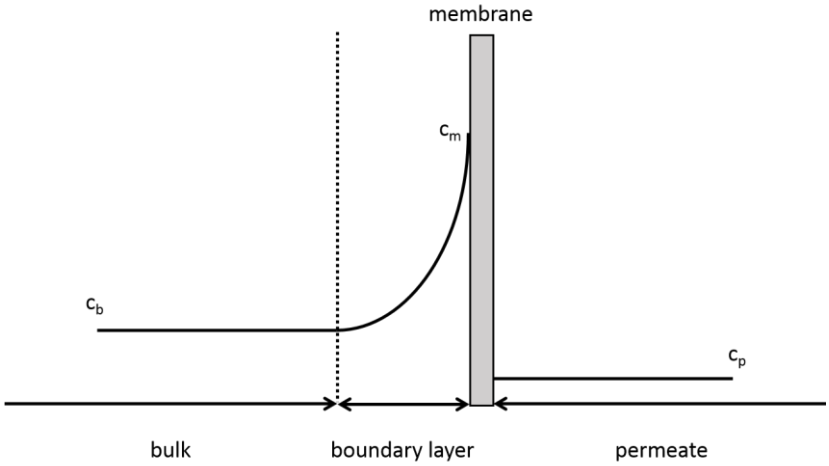

Figure 2. Illustration of concentration polarization in membrane filtration.

2.1.4 Fouling in membrane filtration

Membrane separations offer a separation method with potentially a very low energy demand, but there are limitations to the membrane capacity and efficiency. Deposits on the membrane surface (a surface fouling layer) and deposits inside of the membrane hinders permeate flow. Some operation parameters that affect the fouling are CFV, TMP, particle or solute concentration, fluid viscosity, electrostatic interactions, filtration time and membrane properties.

In addition to R_m and R_{cp}, the fouling related resistance, *i.e.*, resistance from the surface fouling layer or cake (R_c) and pore-fouling (R_p) also pose as extra resistance (Lewis, 2014). Together, they function in series, increasing the total resistance of the system. Therefore, the permeate flux is also described as a resistance model, where all flux-reducing phenomena are included, Eq. 5 (Lewis et al., 2017).

$$J = \frac{TMP - \Pi}{\mu(R_m + R_{cp} + R_c + R_p)} \tag{5}$$

Where Π is the difference in osmotic pressure over the membrane. The osmotic pressure in solutions containing low molecular mass solutes, as in RO and NF, is often high even at low solute concentration, whilst in UF and MF, the osmotic pressure is normally negligible (Strathmann, 2011a).

The cake resistance (R_c), which is the resistance from the formation of a surface fouling layer (or cake) depends on the mass of solid material per surface area and the specific cake resistance (α_c). The specific cake resistance is calculated according to Eq. 6.

$$\alpha_c = \frac{1}{K\rho_s\phi} \tag{6}$$

Where K is the permeability of the cake, ρ_s is the density of the solid material, and ϕ is the solidosity, which is the ratio of the volume of the solid particles in the cake (V_{solid}), and the total volume of the cake (V_{total}), according to Eq. 7.

$$\phi = \frac{V_{solid}}{V_{total}} \tag{7}$$

The solidosity is also related to the porosity (ε), which is the volume fraction of non-solids in the cake, according to Eq. 8.

$$\phi + \varepsilon = 1 \tag{8}$$

2.1.4.1 Models to describe fouling

Fouling occurs from the deposition of material inside or on top of the membrane, and the different fouling phenomena are described as pore blocking, pore constriction and caking. When modelling filtration, normally four models are used to describe fouling: complete blocking, intermediate blocking, standard blocking and cake filtration, presented in Fig. 3 (Hermans, 1936) (Hermia, 1982).

Complete blocking assumes that each particle that reaches the membrane contribute to the blocking by sealing a pore, and that the particles are not on top of each other, Fig. 3a. While intermediate blocking also assumes that a particle reaching an open pore would seal it, other particles can stay on top of it, Fig. 3b. In standard blocking, the particles smaller than the membrane pore enter the pore and deposit onto the pore walls, Fig. 3c. Finally, in cake filtration it is assumed that cake formation occurs on the membrane surface, and the particles neither seal nor enter the pore, Fig. 3d (Hermia, 1982).

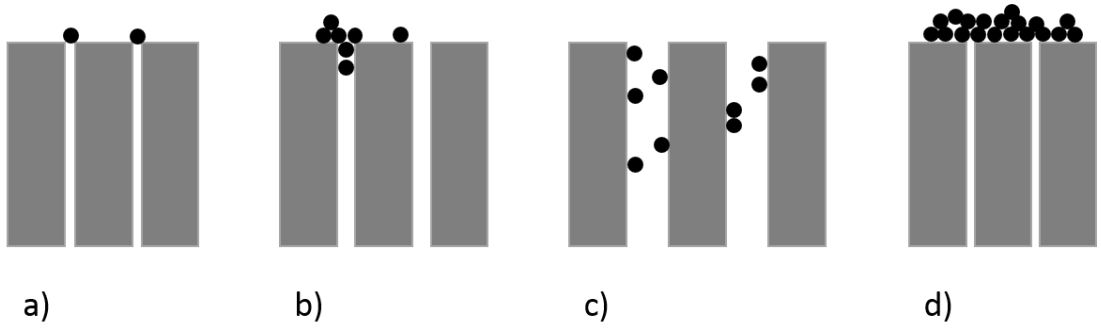

Figure 3. Illustrations of different pore blocking phenomena: a) complete blocking, b) intermediate blocking, c) standard blocking, d) cake filtration.

To describe the flux decline depending on different kinds of fouling, Hermia (1982) developed a general model that can be used for constant TMP filtrations, Eq. 9. The constants, k and n, for the different cases of fouling are presented in Tab. 2. The model was developed for dead-end filtration, but is also useful to model cross-flow filtration, especially in the beginning of the filtration process (Field, 2010).

$$\frac{d^2t}{dV^2} = k\left(\frac{dt}{dV}\right)^n \tag{9}$$

Table 2. Constants for Eq. 5 (Hermia, 1982) for the four different fouling phenomena. Where α_c is the specific cake resistance, c_b is the mass of solid particles per unit permeate volume, σ is the blocked area per unit permeate volume, ϕ_{ads} is the volume of solid particles retained in the pores per unit permeate volume and J_0 is the initial flux through the membrane, explained in Eq. 5 (Lewis, 2014).

Type	k	n
Cake filtration	$\frac{\alpha_c c_{bp} \mu}{A_m^2 TMP}$	0
Intermediate blocking	$\frac{\sigma}{A_m}$	1
Standard blocking	$\frac{2\phi_{ads}}{\delta_m A_m^{0.5}} J_0^{0.5}$	1.5
Complete blocking	$J_0 \sigma$	2

However, fouling is often a combination of the separate mechanisms and other models are developed to take the combination of mechanisms into account (Bolton et al., 2006).

2.1.4.2 Compressible fouling layers

The fouling layer that is formed on the membrane can be either incompressible or compressible. A compressible cake allows particles in the cake to move, whilst the individual particle layers do not move in an incompressible cake. For compressible cakes, a modification of the Darcy equation has been developed by Shirato et al. (1969).

For compressible fouling layers, the local specific cake resistance and local solidosity varies within the cake, depending on the local compressive pressure. This relation is unique for each material, and constitutive relationships are used to approximate the response of the applied pressure for a specific fouling layer. There are many empirical relationships to describe the relation, an example is presented in Eq. 10 and 11 (Tiller and Leu, 1980).

$$\phi = \phi_0 \left(1 + \frac{P_s}{P_a}\right)^{\beta} \tag{10}$$

$$\alpha_c = \alpha_0 \left(1 + \frac{P_s}{P_a}\right)^{n} \tag{11}$$

Where P_a, β, and n are empirical parameters and P_s is the local solid compressive pressure due to drag from skin friction of the liquid on the particles. ϕ_0 and α_0 are also empirical parameters, which can be interpreted as the solidosity and specific cake resistance at no compressive pressure.

In compressible fouling layers, a layer close to the filtration media which contributes to a major part of the pressure drop over the membrane, can appear. The formation of this layer is called skin formation (Tiller and Green, 1973). The actual formation of a skin is hard to prove since it requires *in situ* measurements of local pressure and local solidosity during filtration and these measurements are uncommon and hard to perform. An example of such a study is made by Mattsson et al. (2012).

2.1.5 Critical flux model

For cross-flow filtration, the modelling of membrane fouling rate is made more complex than in cake build-up during dead-end filtration, because some of the fouled particles are resuspended by shear forces from the cross-flow, *i.e.* back-transport (Belfort et al., 1994).

One model that take the back-transport into consideration is the critical flux model. It assumes that there exists a critical flux through the membrane, below which no loss of performance due to fouling will occur (Field et al., 1995). This is valid if the system is started below the critical flux and if the filtration is operated at these conditions, *i.e.* generally low TMP which gives a low flux, the fouling will be negligible. The value of the critical flux depends on the hydrodynamics and surface interactions of the species in the system and the exact value is hard to determine based on theoretical predictions.

Field et al. (1995) proposes a modification of Eq. 9 to adjust to cross-flow filtration where the critical flux, which should not be exceeded, is included, see Eq. 12.

$$-\frac{dJ}{dt}^{n-2} = k(J - J^*) \tag{12}$$

Where J^* is the critical flux, n and k are the same constants as presented in Tab. 2 and varies depending on the blocking mechanism. The same blocking mechanisms as discussed in Section 2.1.4.1 are applied, except standard blocking in which there is no back transport from cross-flow.

To determine the critical flux based on experimental data or to analyse which blocking mechanism that is present in a filtration system with flux decline, Eq. 12 can be written as in Eq. 13.

$$f(J) = -\frac{dJ}{dt}J^{n-2} \tag{13}$$

If $f(J)$ is plotted against J, a linear relation should be obtained. From this relation J^* or the other constants can be estimated, as showed by e.g. (Lewis et al., 2017).

Different theories have been used to account for the back-transport of particles from the membrane surface. One is based on the increased diffusion from particle interactions in shear flow (Eckstein et al., 2006), and the other one is based on the inertial lift force away from the wall that is produced by the velocity gradient (Altena and Belfort, 1984). Li et al. (2000) identified the critical fluxes for different types of supermicron particles and tested those two theories for different particle sizes, in order to find a relation between the cross-flow velocity and the critical flux.

2.2 Fouling layer characterisation

It is crucial to gain more understanding of the membrane fouling phenomena in order to optimise the operation of membrane filtration equipment. To investigate the fouling behaviour and determine parameters to the models described in Section 2.1.4, it is important to perform experiments and to have reliable techniques to measure all variables needed. Variables that are considered to be of importance are the thickness of the fouling layer along with measures of the degree of different fouling phenomena.

The most straightforward method to examine the fouling layer is to recover the fouled membrane after filtration, then the amount of deposits and structure of the fouling layer can be studied. Disadvantages of this kind of examination are the difficulty of taking out the fouling layer at an exact time and to do it without damaging it. To instead enable measurements *in situ* and in real time, several different techniques have been applied. Direct observation by using a microscope and a camera to monitor the

deposition of particles have been used in some studies, including (Li et al., 1998). Others have used laser beams, where the angle of the reflected beam can be used to calculate the variation of height of a surface, to study the growth of fouling layers, e.g. (Schluep and Widmer, 1996). Mairal et al. (1999) were the first to use ultrasonic measurements in microfiltration, where sound waves reflected against the fouled surface. These are some of the *in situ* methods that are used in the characterisation of membrane fouling, and they all have both advantages and limitations. Some difficulties coming up when using these methods are that it may interfere with the fouling, problems with opaque feed suspensions and requirement of knowledge of certain parameters (Lewis et al., 2012).

2.2.1 Fluid dynamic gauging

Fluid dynamic gauging (FDG) is a method that can be used for the measurements of thickness and strength of soft deposits on solid surfaces. The technique was first developed by Tuladhar et al. (2000) who measured the thickness of soft deposits on a solid surface *in situ*. The method is based on fluid mechanics, more specifically pressure drop through constriction. In Fig. 4, a schematic of a FDG gauge is presented. It consists of a tube with a nozzle which is mounted with short distance to the fouled surface. The surface is covered by liquid, which is sucked up through the nozzle due to a pressure difference between the surrounding liquid and the interior of the tube, $\Delta p_{14.}$ The principles of the technique have been used earlier, but with ejection of air towards the surface instead (Jackson, 1978), it can also be used with ejection of a liquid instead of suction (Salley et al., 2012).

There are many variations in FDG setups, to accommodate different fields or to improve accuracy. The first use of FDG for cross filtration microfiltration was made by Jones et al. (2010) who studied the fouling of industrial beet molasses, they found that the gauge flow should neither be affected by the permeate flux nor disturb the permeate flow (Jones et al., 2010). Lewis (2014) developed this technique further to refine the operational procedure and used a range of different foulant materials with different characteristics (Lewis et al., 2016) (Mattsson et al., 2017). Others have also used it for investigation of soft deposits in food industry and how drying affects the strength and required cleaning of the deposits (Chew et al., 2004b) and for investigation of deposits on heat transfer surfaces (Chew et al., 2005). In this study, FDG is used for measurement of membrane fouling layers in cross filtration microfiltration.

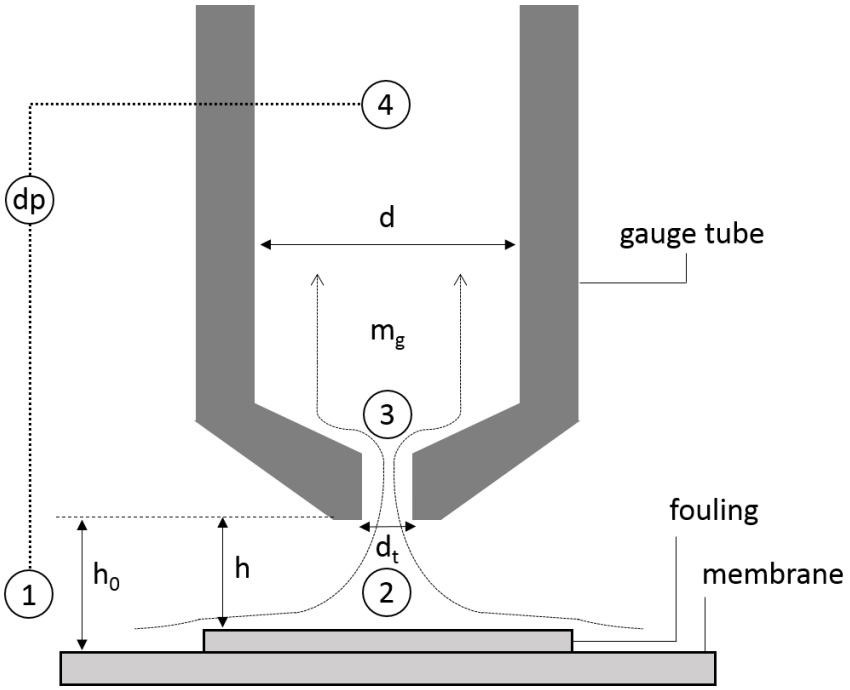

Figure 4. Schematic of an FDG tube, where m_g is the gauge flow rate, d_t is the nozzle diameter, d is the tube diameter, h_0 is the distance from the nozzle to the membrane and h is the distance from the fouling layer to the nozzle. The points 1-4 represents different flow locations.

The pressure difference and the flowrate of liquid through the nozzle is related to the distance from the membrane surface (h_0). When a fouling layer is built-up on the surface, this will instead be related to the distance from the nozzle to the surface of the fouling layer (h), *i.e.* the clearance. The thickness of the built-up layer (δ) can then be calculated according to Eq. 14 (Tuladhar et al., 2000).

$$\delta = h_0 - h \tag{14}$$

The different flow points (1-4) marked in Fig. 4 represent regions between which the pressure difference is important for the understanding of FDG. Point 1 is in the surrounding liquid and point 4 is an arbitrary point where the flow has become laminar and fully developed in the gauge tube. This pressure difference can be measured by a pressure transducer. Between point 1 and 2, the flow is limited by the clearance of the gauge tube from the fouling layer and between point 2 and 3, the nozzle diameter (d_t) is limiting the flow (Lewis et al., 2012).

The original operation mode for FDG, described by Tuladhar et al. (2000), operates with constant Δp_{14} and measures the gauging flow rate (m_g). A disadvantage with this operation mode is that the flow rate of liquid that is withdrawn by the gauge tube varies and a large loss of liquid from the system can imply problems with keeping a constant pressure. Another operation mode is to keep a constant flowrate of the liquid withdrawn through the gauge tube and instead measure the pressure difference over the nozzle, Δp_{14} (Gu et al., 2011). Then the overall flow conditions are less affected by the withdrawn liquid.

If either Δp_{14} or m_g is kept constant and the other one is measured, the measured parameter can be used to calculate the constriction coefficient (C_d), Eq. 15. C_d shows the relation between the actual mass flowrate and the ideal mass flowrate through a circular pipe and is derived according to the Bernoulli equation.

$$C_d = \frac{m_g}{\frac{\pi d_t^2}{4}\sqrt{2\rho_L \Delta p_{13}}} \tag{15}$$

Where d_t is the diameter of the nozzle, ρ_L is the density of the fluid and Δp_{13} is the pressure difference between location 1 and 3 in Fig. 4. Δp_{13} cannot be directly measured and needs to be calculated from Eq. 16, which is developed from the Hagen-Poiseuille equation and assumes laminar flow in the gauge tube.

$$\Delta p_{13} = \Delta p_{14} - \Delta p_{34} = \Delta p_{14} - \frac{128 \mu m_g l_{eff}}{\pi d^4 \rho_L} \tag{16}$$

Were μ is the viscosity of the fluid, l_{eff} is the effective length of the gauge tube between point 3 and 4, and d is the diameter of the tube. By making measurements with a non-porous surface, a relation between C_d and h/d_t can be estimated. This relation can then be used to determine the clearance for a surface with deposits.

There are thus only two varying parameters, m_g and Δp_{14}, and Eq. 15 and 16 provides a relation between them. So, to simplify calculations, a relation of Δp_{14} – h/d_t or m_g – h/d_t can be used instead of C_d - h/d_t, to determine the clearance for a surface with a fouling layer. Δp_{14} is hereafter referred to as simply Δp.

A general curve from experimental measurements of Δp against h/d_t is presented in Fig. 5. It can be seen that in the region relatively close to the surface, where h/d_t is below 0.25, Δp is the most sensitive to h/d_t and at higher values of h/d_t, Δp tends to an asymptotic value. Δp depends on the gauge flow rate, the nozzle diameter and the clearance. The dependence on clearance becomes more important when the clearance decreases. The region where $h/d_t < 0.25$ is called the incremental zone and thickness measurements should be carried out in this region in order to get reliable results (Tuladhar et al., 2000).

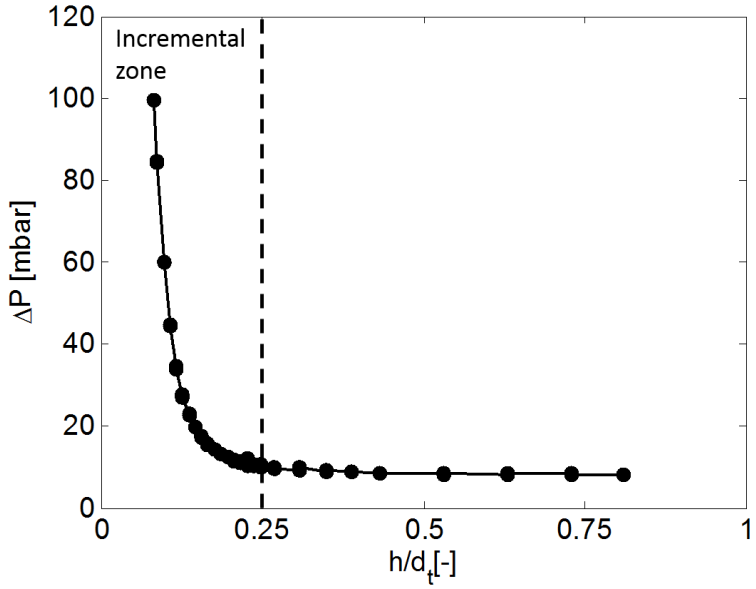

Figure 5. A general curve of Δp vs h/d_t, experimentally obtained from measurements with d_t = 500µm and m_g= 0.1g/s. The incremental zone, $h/d_t < 0.25$, is marked by the dashed line.

By this relationship between Δp and of h/d_t, the thickness of a fouling layer can be calculated from FDG measurements on the fouled surface and Eq. 14.

However, it should be noted that FDG is not an entirely non-invasive method, since the shear stress on the surface caused by the suction of liquid can cause destruction of the surface fouling layer.

2.2.1.1 Strength measurements

Another application of FDG is to measure the cohesive strength of the fouling layer by estimating the maximum shear stress that can be applied to the fouling before parts of the fouling layer is removed. Further down in the fouling layer, the same method can also measure the adhesive strength between the fouling layer and the membrane. This application was first described by Chew et al. (2004a) who performed CFD simulations to estimate the maximum shear stress ($\tau_{w,max}$) applied to the fouling layer related to the nozzle shape. The area just below the inner radius of the nozzle is exposed to the largest shear stress (Chew et al., 2004b) and an analytical model, Eq. 17, was found to agree with results from CFD simulations (Chew et al., 2004a) (Chew et al., 2004b) (Gu et al., 2009). The shear stress (τ_w) on the surface below the nozzle can be estimated using the Navier-Stokes equation, assuming creeping concentric flow between parallel plates.

$$\tau_{w,max} = \frac{6\mu m_g}{\rho_L \pi h^2}\left(\frac{1}{d_t}\right) \tag{17}$$

The assumption is valid if the criteria in Eq. 18 is fulfilled (Fryer et al., 1985).

$$\frac{m_g h}{12\rho_L \pi d_t \mu} \ll 1 \tag{18}$$

2.3 Microcrystalline cellulose

Cellulose is the main component in wood material and microcrystalline cellulose (MCC) is a purified form of cellulose. Cellulose is a polysaccharide of glucose consisting of two consecutive glucose anhydride units (cellubiose), linked by 1,4-β-glycosidic bonds. The beta linkage gives linear molecules that are ordered in sheets, bonded together by hydrogen bonding as well as hydrophobic interactions. Fig. 6 shows the molecular structure of cellulose, where *n* can range from about 50 in processed forms to about 12,000 in natural forms. The polysaccharide is insoluble in water and dilute acids at ordinary temperatures. MCC swells in water and the shape of the particles varies considerably, but they can to some extent be considered cylindrical.

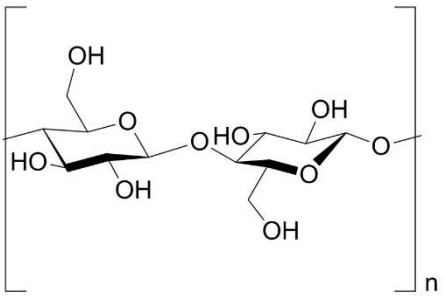

Figure 6. Molecular structure of cellulose.

Paper pulp is commonly used as raw material for the production of MCC. The pulping process is used to remove lignin, other polysaccharides and extractives. The products from this step are fibres that contains amorphous and crystalline parts. The amorphous parts are removed by strong mineral acid hydrolysis and the remaining crystalline parts are purified by neutralization, washing and filtration and then diluted in water and spray-dried to obtain non-colloidal MCC (Phillips and Williams, 2009).

MCC has been used for several years to achieve physical stability and texture modification in many food applications. In this study, MCC is used as a model material for dewatering of small cellulosic particles, which is of interest in the development of biorefineries.

2.3.1 Electrostatic interactions in MCC

In order to investigate the impact of different pH on a MCC suspension, Wetterling et al. (2017) measured the surface charge of MCC at different pH, by titration with a linear pDADMAC (polydiallyldimethylammonium chloride). At neutral conditions the surface charge of the MCC particles was about -0.75 µg pDADMAC eq. g^{-1}, while for pH 2.9 the charge is close to zero due to protonation of most of the carboxylic groups in the cellulose. If there would be any surface charge on the MCC after addition of acid, the charges would also be shielded by the added ions and this would obstruct the interaction between MCC particles.

Mattsson et al. (2012) performed experiments on dead-end filtration of MCC with different membranes (hydrophilic polyethersulfone, hydrophilic regenerated cellulose membrane and cellulose nitrate membrane) with a pore size of 0.45µm and different pH levels (2.9, 3.8 and 6.3), and concluded that skin formation is largely depending on electrostatic interactions between both particles and filter medium. Their results showed that the MCC filter cakes are compressible and that a lower pH show a lower filtration resistance. There were also indications of skin formation for some operation conditions. The pores of the membrane were blocked by a skin layer with the thickness of less than 1 mm or an even thinner skin layer, consisting of single particles.

3 Experimental

3.1 Filtration experiments

Below follows descriptions of the experimental setup, the experimental conditions and the procedure in which the experiments were carried out.

3.1.1 Experimental setup

An illustration of the flow loop for the filtration experiments and FDG measurements is shown in Fig. 7, the feed is pumped by a gear pump (MCP-Z, Ismatec) into the flow cell and the retentate is recirculated back to the feed tank.

As mentioned in Section 2.1, membrane filtration can be carried out either with constant TMP or constant flux. In this study, constant TMP is applied since it is easier to control in this equipment, it is measured by pressure meter P and manually adjusted by valve V3, Fig. 7. The gauge flow is withdrawn from the main flow, and is kept constant (with an accuracy of ±0.2 % of the mass flow) by a pump followed by a control valve with a flow meter (Mini CORI-FLOW, Bronkhorst). The pressure pulses from both the feed pump and the gauge pump were reduced by air dampeners (dmp) after the pump outlet. The gauge flow is drained during experiments, but because of the low gauge flow rate, the drained volume is negligible. The feed tank has a volume of 25L with a diameter of 295 mm, it is baffled and stirred by a pitched blade impeller with two blades and a diameter of 165 mm, with a stirring rate of about 200 rpm.

a)

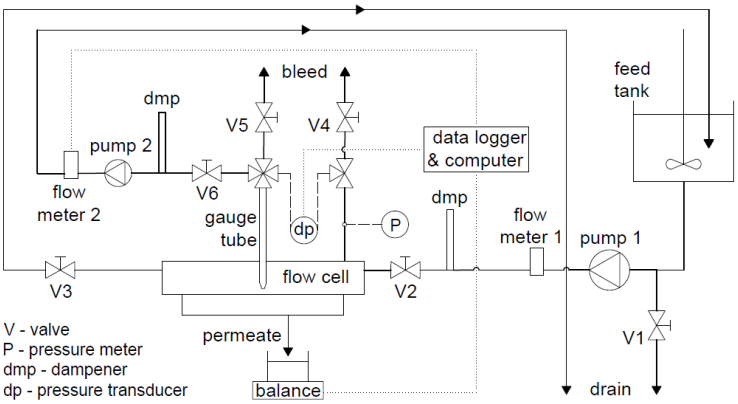

b)

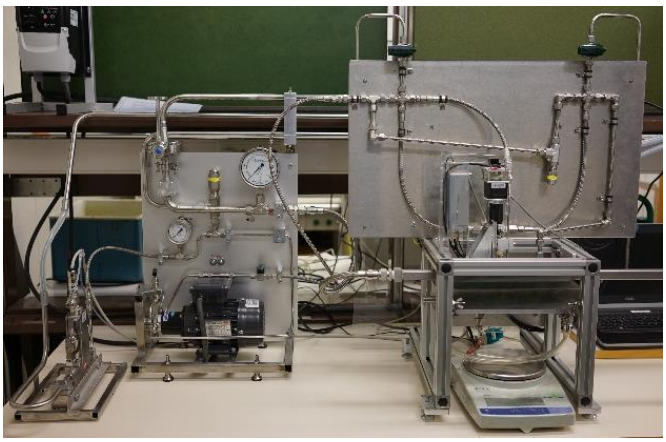

Figure 7. The flow loop used for the filtration experiments and FDG measurements. a) schematic illustration of the flow loop (illustration adapted from (Zhou and Mattsson, 2018)), b) photo of the flow cell and gauge system, the feed tank and pump is not included (photo by Hans Theliander).

A schematic illustration of the flow cell and the FDG equipment is shown in Fig. 8. The position of the gauge tube (*h*) is controlled by the stepper motor. The gauge tube is attached to a clamp, which is connected to a screw thread that moves when the stepper motor rotates, this allows the gauge tube to move up and down in the flow cell. One step in the stepper motor corresponds to 0.9°, which gives a linear movement of the gauge tube of 2.5 µm. However, the stepper motor can take as small as 1/8 of a step, which gives a linear movement of 0.3125 µm. The rotation of the stepper motor also adjusts a linear potentiometer (PT) via a gearing system on top of the stepper motor, this gives a rough measurement of the position of the gauge tube. To get an even more accurate reading of the position of the gauge tube, a linear variable differential transformer (SM-series LVDT, Singer-Instruments) is used. The LVDT consists of a stationary part and a rod that moves in and out of the stationary part with the movement of the gauge clamp. The movements produces an induction current with a voltage proportional to the position of the rod (Lewis, 2015). By knowing the position of the gauge tube, a value of *h* can be logged. To get a value of Δp, a pressure transducer (PX419-2.5DWUV, Omega) measures the difference in pressure in the flow cell and in the gauge tube, this is indicated as dp in Fig. 7.

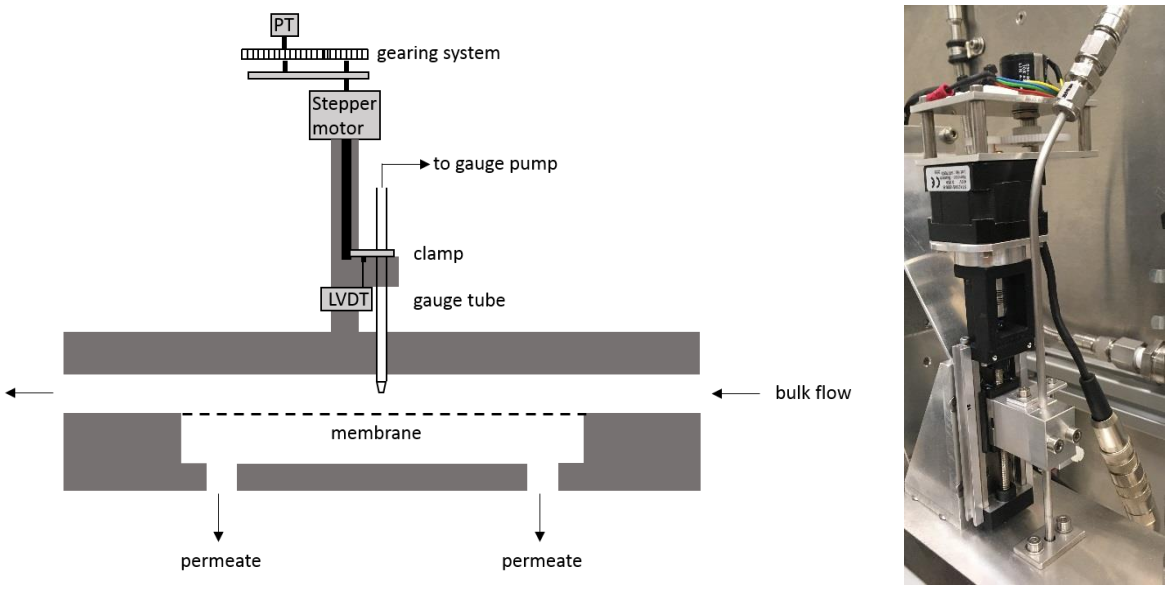

a) b)

Figure 8. a) Schematic illustration of the flow cell and gauge tube. b) Photo of the gauge tube, LVDT, stepper motor and potentiometer.

3.1.2 Materials and experimental conditions

For all experiments, MCC (Avicel PH-105) was suspended in deionized (DI) water and homogenized by using an IKA Ultra-Turrax® T50 with the dispersing element S50 N-G45F during 15 min at a rotational speed of 10,000 rpm. Before filtration experiments, the suspension was stirred overnight. For all filtrations 15L of 0.02 vol% MCC suspension was used. The same material and pre-treatment was used by Zhou and Mattsson (2018), then the particle sizes ranged from 1.5 to 91.2 µm.

Two different membranes were used in the experiments, one hydrophilic regenerated cellulose membrane with 0.2 µm nominated pore size (RC58, GE Whatman) and one hydrophilic polyethersulfone filter (Supor ®, Pall Corporation) with nominated pore size of 0.45 µm. The

regenerated cellulose membrane has a clean water flux of 0.57 ml s^{-1} cm^{-2} at TMP = 0.9 bar and the polyethersulfone membrane has a clean water flux of 0.97 ml s^{-1} cm^{-2} at TMP = 0.7 bar, according to the manufacturers. The same membrane types, but all with pore size of 0.45 µm have been used by Mattsson et al. (2012) to investigate the filtration properties of MCC in dead-end filtration. They also measured the surface charge of the membranes and found that at neutral conditions the regenerated cellulose membrane have a charge of -1.7 µ eq. g^{-1} and the polyethersulfone membrane have a surface charge of -0.8 µ eq. g^{-1}. At pH 2.9 the surface charge was close to zero for both membranes.

Since the membranes swell in water, the one to be used in the filtration was soaked in DI water in advance to get fully swollen and just before the filtration experiment it was mounted in a cassette which was placed inside the flow cell. The cassette consisted of 4 layers, the top layer was the actual membrane which was followed by three supporting layers: a hydrophilic polyethylene sheet with pore size of 20 µm (Porex, Germany) and two layers of metal mesh (0.25 mm and 2 mm in pore size, respectively). The active membrane surface was 16×150 mm.

The cross-flow velocity was set to ~4 L min^{-1} for all experiments, this corresponds to turbulent flow of Re = 4170 for the flow that enters the flow cell. The Reynolds number (Re) decreases a little bit along the membrane, due to the permeate flux. In the beginning of the filtration, Re decreases more along the membrane, since there is no fouling and the permeate flux is high. Then Re reaches around 4000 in the middle of the membrane. In the end of the filtration, there is more fouling and a lower permeate flux, then Re decreases less along the membrane. The temperature of the filtered suspension was within 22-24°C and the gauge flow was kept constant at 0.1 g s^{-1}. TMP was kept at 200mbar (±5%) with larger variations in the initial filtration stages and smaller variations in the latter stages.

To investigate the effect of surface charge of the particles and the membrane, filtration experiments were performed at two different pH levels, 2.9±0.05 and 6±0.6. The larger variation in pH at the higher pH level is because of variations in pH of the DI water from the tap. For the experiments with acidic conditions, pH was adjusted by addition 1.7±0.05 ml of 6 M sulfuric acid (H_2SO_4) to 15L water and MCC, the amount was depending on the initial pH of the water.

3.1.3 Permeate flux

During the whole experiment, including clean water filtration, MCC filtration and FDG measurements, the permeate flux was measured by collecting the permeate in a container standing on a balance. The weight data is logged each second. The container holds ~2.7L and when it was filled up, the permeate was poured back into the feed tank.

3.1.4 FDG measurements

To get accurate results for each FDG measurements, some steps were required before the actual measurements of the fouled membrane surface could be conducted. The steps are described below. Calibration was only performed after disassembling of the FDG equipment, but the membrane position had to be controlled in each experiment.

3.1.4.1 Calibration

To obtain a relation between Δp and h/d_t, as mentioned in section 2.2.1, measurements of Δp with known distances from the surface were needed. This was performed by using a stainless-steel plate in the flow cell instead of a membrane. DI water was used for the cross-flow. The gauge tube was put in contact with the steel plate, a multimeter was used to measure the electrical resistance to verify contact, and the distance was set to be equal to zero. Then the position of the gauge tube was changed in small steps and the pressure drop over the gauge tube were logged for the different distances from the solid surface, resulting in a calibration curve like the one in Fig. 5. The gauge flow rate was kept constant during all

measurements, and since it gets harder for the pump to maintain a constant flowrate when the flow resistance is larger, the calibration was stopped when Δp exceeded 100mbar.

3.1.4.2 Membrane position

With a membrane instead of a solid plate, the position of the surface changes slightly since the membrane is soft and is placed in the flow cell manually before each experiment, and to get accurate thickness measurements, the change in position must be accounted for in the calculations. To do this, similar measurements were performed as for the calibration curve. The membrane calibration curve was plotted together with the calibration curve and h/d_t values of the membrane calibration curve are adjusted with a offset value, $h_{0,offset}$, to overlap the main calibration curve, this is illustrated in Fig. 9.

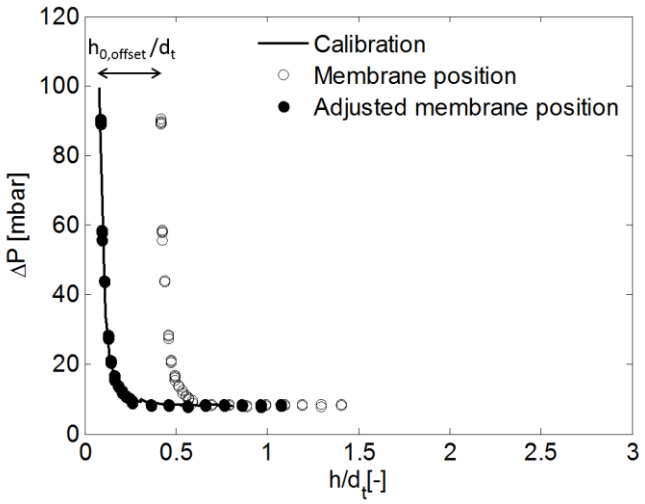

Figure 9. Calibration curve along with measurements of the membrane position. The unfilled markers show the membrane position and the filled markers show the membrane position after adjusting with the $h_{0,offset}$ value.

3.1.4.3 Strength and thickness measurements

Before adding MCC to the feed flow, the stirrer was started and the gauge tube was positioned high up in the flow cell to disturb the flow as little as possible. When adding MCC in the feed flow the fouling of the membrane started immediately which results in an increase in TMP. To compensate for the increase in TMP, valve V3 in Fig. 7, after the flow cell was opened carefully and gradually so that the TMP could be kept constant. After 1000 s undisturbed filtration, the FDG measurements started. Then the FDG tube was lower down in the flow cell and hindered the deposition of particles on the membrane in the measuring area. A similar set of measurements were performed as for the membrane calibration, described in Section 3.1.4.2, until Δp exceeded 100mbar. The collected data was processed as described in Section 3.1.4.4 and adjusted with the same $h_{0,offset}$ value as the curve for the membrane position. If the pressure increased with the same slope as for the calibration curves, when moving the gauge tube closer to the fouled surface, the fouling layer resisted the shear stress applied by the gauge flow. If the shape of the Δp - h/d_t curve instead differed from the calibration curve, parts of the fouling layer had been sheared off. In this way, the strength of the fouling layer can be measured locally at different heights in the fouling layer, all through the destruction of the fouling layer.

To get a comparable value of the thickness of the fouling layers, it needs to be measured at the same distance from the fouling layer in every experiment, so that the shear stress from the suction of fluid is the same in every measurement. This gives a value of the thickness at which the fouling layer is strong enough to resist that shear stress. In this study, the thickness measurements are made at $h/d_t = 0.2$, which

is in the incremental zone, it corresponds to a fluid shear stress of 35.7 N m^{-2} on the fouling layer, calculated from Eq. 17.

3.1.4.4 Data processing

From the calibration curve, explained in section 3.1.4.1, a function of Δp depending on h/d_t was derived, Eq. 19, by using the Curve Fitting Toolbox ™ in MatLab.

$$\Delta p = c_1 exp(\frac{c_2}{h/d_t}) + c_3 exp(\frac{c_4}{h/d_t}) \quad (19)$$

Where c_1 = 1135.34, c_2 = -1.57, c_3 = 2.58 and c_4 = 0.302. A figure of the fitted curve and the calibration data is presented in Fig. 10. To get the best fit, the fitting starts at h_0/d_t equal to 0.25, in the incremental zone, described in Section 2.2.1. Calibration data is accessible up to Δp = 99.3 mbar, and the model cannot be extrapolated. The R^2 value of the regression model is 0.9990 and R^2_{adj} is 0.9989.

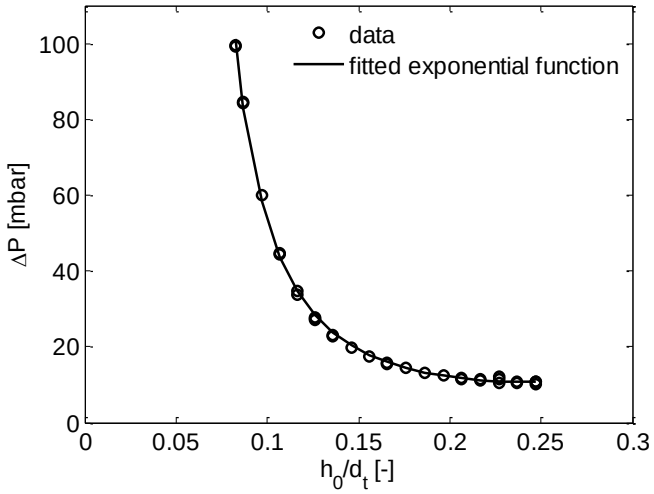

Figure 10. Plot of calibration data and fitted exponential function, Eq. 19, in the incremental zone.

By using the built-in MatLab function "fsolve", the regression model is solved for h/d_t with the Δp values logged for the FDG measurements with a fouling layer present, described in section 3.1.4.3. The remaining thickness of the fouling layer can be calculated from Eq. 14 and the logged values of h_0/d_t. The first data that is used for thickness calculations, is where the gauge flow already applies a shear stress of 35.7 N m^{-2} on the fouling layer, and the estimated thickness is thus the thickness remaining with the application of this shear stress.

3.1.5 Fouling layer recovery

To finish the filtration experiment, the feed pump was stopped and the valves V2 and V3 (Fig. 7) before and after the flow cell were closed. The feed suspension remaining in the flow cell was forced out by injecting air with a syringe and keeping the same TMP as in the filtration. The amount of liquid that came out was measured.

The lower part of the flow cell was removed and the membrane with the filter cake was collected carefully. About one third of the cake was used for solidosity and surface weight calculations, one third was used for particle size measurements and the last third was stored in a freezer to enable for further studies in the future.

3.1.6 Cleaning of equipment

After the recovery of the fouling layer, the membrane was replaced by a metal plate and the flow system was rinsed three times with clean DI water. The feed pump was run with high flow, to remove as much particles as possible from the walls of the flow cell and from the pipes.

3.1.7 Surface weight

The time required for FDG measurements varied between experiments, so the surface weight also varied since the filtration continued during those measurements. To get accurate results for the surface weight, separate filtration experiments without FDG measurements were performed. The surface weight gives an actual measure of the amount of particles in the fouling layer and do not depend on the compression of the fouling layer, as is the case for thickness measurements.

To get similar conditions as for the FDG measurements, the filtration was run with only DI water for 30 min, which was the average time for the FDG procedure described in Section 3.1.4.2. Then MCC was added and filtration was carried out for 1000 s, before following the same procedure to recover the fouling layer as described in Section 3.1.5. If a part of the fouling layer got damaged during the recovery it was taken away, and the remaining fouling layer was dried in an oven (105 °C), weighed and used to calculate the surface weight. The calculations are shown in Appendix I.

3.2 Particle characterisation

The size of the MCC particles in the suspension is of importance to understand the fouling behaviour. The exact size and shape of the particles is not known, but the two methods described below gives an insight of the size distribution.

3.2.1 Laser diffraction

The size of the particles in the feed suspension and in the cake was measured after each experiment. This was performed by laser diffraction (Mastersizer 2000, Malvern Instruments). The detection range of the equipment is 0.02 – 2000 µm.

3.2.2 Focused beam reflectance measurement

To investigate whether the particle size of MCC changes in acidic conditions compared to unadjusted conditions, focused beam reflectance measurement (FBRM) was used. FBRM measures the chord length distribution of the particles *in situ* by sending out a focused laser beam in the suspension and detecting the reflections. The FBRM has a detection range of chord lengths of 1 - 1000 µm and can be used at higher particle concentrations than the laser diffraction.

Two FBRM measurements were performed in this work, one with the same concentration as in the filtration experiments (0.02%) and one with higher concentration (0.15%). The higher concentration was used to get a more statistically reliable result since the results will be based on a larger amount of particles. The measurements were carried out in a vessel with initial stirring of 200 rpm, but with different dimensions than the feed tank in the filtration flow loop. For the 0.15% measurements, the initial pH was unadjusted, then base (NaOH) was added to pH 10. Following, acid was added until pH below 2.9, in this state the stirring was increased to 400 rpm for a while and then decreased to the initial settings. Data points of the chord length and number of particles were logged continuously every fifteenth second.

3.3 Sedimentation

Two separate simple sedimentation tests were carried out, one test to compare the sedimentation velocity in a suspension at pH 2.9 with a suspension with unadjusted pH, and one test to compare the sedimentation in suspensions with different ionic strength. For the test with ionic strength, an equal amount of salt (Na_2SO_4), as the amount of acid (H_2SO_4), was added to one suspension, and ten times

more salt was added to the other suspension. The test with ionic strength was carried out in order to investigate whether the same effects would appear with only the shielding of the surface charges, as when the surface charge was removed and there were shielding from ions in the acid.

For the tests, two identical 1000 mL cylinders were used and put in front of a coloured background, to allow easier visual detection of changes in opacity of the suspensions. Two suspensions of 0.15% were prepared as described in Section 3.1.2. After adjusting pH or ionic strength, the two suspensions were poured into the cylinders at the same time and changes in opacity were studied visually and documented by taking photographs. Documentation was made on shorter intervals in the beginning and longer intervals in the end. Samples were taken in the middle of each cylinder, for the test with adjustment of pH, after 48h and 52h. For the test with adjustment of ionic strength, the samples were taken after 25h and 29h. On these samples, the particle size distribution was measured by laser diffraction, in order to control if particles were still settling. The sedimentation tests were stopped when there were negligible changes in suspended particle size over time.

To adjust pH, 0.200 ml 6 M sulfuric acid was added to a 2L MCC suspension. To adjust the ionic strength 2 ml and 20 ml, of a 0.6 M sodium sulphate (Na_2SO_4) solution, were used respectively for two MCC suspensions. Sulfuric acid has two hydrogens and thus two pK_a values. Since $pK_{a,2}$ for sulfuric acid is around 2, it is assumed that the acid is mostly dissociated at pH 2.9. So to get approximately the same ionic strength in the suspension with salt, as is achieved when adding acid to get a pH 2.9 suspension, the same amounts of sodium sulphate and sulfuric acid were used.

4 Results and discussion

In this section the experimental results are presented and discussed. First the flux is compared, then the different results from the FDG measurements are presented, along with results from the separate surface weight measurements. This is followed by results from laser diffraction and FBRM, finally the results from the sedimentation tests are shown.

4.1 Permeate flux

For all filtration experiments, the permeate flux was recorded both during pure water filtration and with MCC in the feed. The flux profiles for experiments with FDG measurements are presented in Fig. 11, the regenerated cellulose membrane is shown in Fig. 11 a, and the polyethersulfone membrane is shown in Fig. 11 b. The flux profiles for the surface weight experiments look similar and can be found in Appendix II.

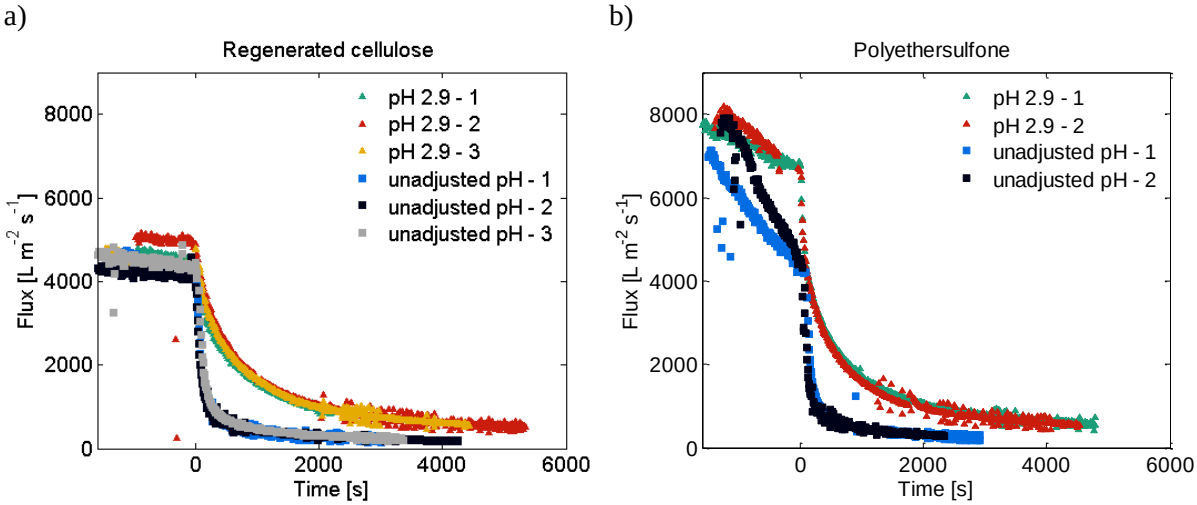

Figure 11. The flux through the membranes over time. The time axis is adjusted to be zero at the time for addition of MCC to the feed. The triangles indicate pH 2.9 and the squares indicate unadjusted pH. a) Regenerated cellulose membrane, three replicates at each pH. b) Polyethersulfone membrane, two replicates at each pH.

The MCC is added to the feed flow at time zero and there is an obvious difference between the two pH levels in the development of the flux from this point. The ones at unadjusted pH have a steep decrease that almost flattens and reaches a rather steady low flux relatively fast. The experiments at pH 2.9, on the other hand, have a slower flux decrease and do not reach the same low level during the time of filtration. This pattern is similar for both membranes. This difference in the initial phase of MCC filtration indicates that there is a difference in fouling mechanisms (described in Section 2.1.4.1) at the two pH levels. There are no particles that are small enough to enter the membrane pores, so it cannot be standard blocking for any of the pH levels. The strong decrease for the case with unadjusted pH indicates that the pore openings of the membrane are blocked and may be sealed while for the pH 2.9 experiments the slower decrease indicates cake filtration and that the pores are not completely sealed. From these results it is probable that there is a difference in particle size for the two pH levels. They are both treated in the same way, but the elimination and shielding of surface charge at pH 2.9 could cause agglomeration of the MCC particles.

When comparing the two membranes, it can be seen that the initial flux with pure water is higher for the polyethersulfone membrane, and this is expected from the pure water flux specifications given by the manufacturers, see Section 3.1.2. The flux decrease during pure water filtration is probably due to MCC

remaining in the equipment even after cleaning. Especially for the polyethersulfone membrane it is obvious that the flux decrease during clean water filtration is larger for unadjusted pH. Assuming that the amount of MCC is the same each time during clean water filtration, this also indicates that the pores are blocked or sealed by the MCC particles at unadjusted pH. The initial flux is higher for the polyethersulfone membrane, so more particles reaches the membrane and can seal the pores, therefore the flux decrease is steeper for this membrane than for the regenerated cellulose membrane.

4.2 FDG measurements and surface weight

For the regenerated cellulose membrane, three replicates of FDG measurements at each pH level were performed and for the polyethersulfone membrane, two replicates were conducted at each pH level. At the first data point of Δp - h/d_t that is used, some particles may have been sheared off already, since a fluid shear stress of 35.7 N m^{-2} is then applied to the surface. However, it gives the thickness at which the fouling layer is strong enough to resist the shear stress of 35.7 N m^{-2}.

These resulting thicknesses of the fouling layers formed at the regenerated cellulose membrane and the polyethersulfone membrane are reported in Tab. 3 and 4 respectively.

Table 3. Remaining thickness after shear stress of 35.7 N m^{-2} on the fouling layers formed with the regenerated cellulose membrane. Three replicates at each pH.

pH	Thickness [µm]		
2.9	606	738	661
unadjusted	378	232	264

Table 4. Remaining thickness after shear stress of 35.7 N m^{-2} on the fouling layers formed with the polyethersulfone membrane. Two replicates at each pH.

pH	Thickness [µm]	
2.9	775	757
unadjusted	147	189

There is a limited difference between the thicknesses of the fouling layers for the two membranes, even though the surface structure and pore size were different. But for both membrane types there is a clear difference between the pH levels, experiments run with pH 2.9 forms considerably thicker fouling layers than the ones formed at unadjusted pH. A reason for this might be that there are repulsive forces from the surface charge, both between particles and between particles and the membrane, at unadjusted pH. This may facilitate the removal of particles from the fouling layer, by the shear stress from the cross-flow. At pH 2.9, there are no such repulsive forces and the particles can be more densely packed together into a thick fouling layer. Another reason is probably that with less pore blocking, as for the experiments at pH 2.9, the permeate flux is higher during a longer time period and more particles are transported to the membrane surface. If there is a difference in sedimentation speed between the two pH levels, it could also affect the fouling layer thicknesses.

The difference in thickness can also be visually observed when taking out the membranes with the fouling layers from the flow cell. In Fig. 12 there are one photo for each pH and membrane, of the membrane and fouling layers after FDG measurements. The FDG probe approaches the membrane in the middle, which can be seen from the destruction of the fouling layer on all photos. The flow has gone from right to left on the membrane and it can be seen that the flow around the probe affects the build-

up of particles downstream, especially on Figs. 12a and c. Some of the destruction of the fouling layers, seen in Fig. 12, comes from back flow of water through the gauge tube and the injection of air, when recovering the fouling layer, as described in Section 3.1.5.

Figure 12. Photos of the membranes and fouling layers after FDG measurements. a) pH 2.9, regenerated cellulose membrane, b) unadjusted pH, regenerated cellulose membrane, c) pH 2.9, polyethersulfone membrane, d) c) unadjusted pH, polyethersulfone membrane

The results from the separate surface weight experiments are presented in Tab. 5 and 6, the surface weights are from separate experiments with the same conditions as the experiments with FDG measurements. Three replicates were made at each pH, with each membrane. As expected from the previous results, there is a noticeable difference between the experiments with low pH and the unadjusted pH, with more particles in the thicker fouling layer and fewer particles in the one with unadjusted pH.

Table 5. Surface weight for fouling layers with regenerated cellulose membrane. Three replicates at each pH.

pH	Surface weight [kg m^{-2}]			Average
2.9	0.22	0.23	0.21	0.22
6.3	0.04	0.03	0.04	0.04

Table 6. Surface weight for fouling layers with polyethersulfone membrane. Three replicates at each pH.

pH	Surface weight [kg m^{-2}]			Average
2.9	0.21	0.24	0.23	0.23
6.3	0.04	0.04	0.05	0.04

Figure 13 shows photos of the polyethersulfone membrane with fouling layer from surface weight experiments. Compared to the fouling layers in Fig 12, it can be seen that this fouling layer was much

more intact in these experiments, since no FDG measurements were performed. The result is similar for the regenerated cellulose membrane.

a)

b)

Figure 13. Photos of membranes and fouling layers from surface weight experiments. a) pH 2.9, polyethersulfone membrane b) unadjusted pH, polyethersulfone membrane.

In Fig. 14 four sets of FDG curves are presented, for the two different membranes with the two different pH levels. The curves only show the results from one replicate for each case, but the shapes of the curves are representative for each membrane and pH level and the curves for the remaining replicates can be found in Appendix III. The yellow line represents measurements on a fouled membrane, and its position along the x-axis gives a measure of the distance of the probe from the membrane and hence the thickness of the fouling layer remaining on the membrane. The difference in thickness between the two pH levels, discussed above, is easily seen in the figures.

The shape of the yellow line indicates the strength of the fouling layer, in a sense that if it has the same shape as the other two lines in the figure, the fouling layer can resist the shear stress that is applied to it. When Δp increases, the shear stress also increases, according to Eq. 17, and when a part of the fouling layer shears off, Δp drops since the resistance for the gauge flow decreases. This can be seen on the drops of the yellow line. By comparing the measurements for low pH and unadjusted pH (Fig. 14a vs b and Fig. 14c vs d) it can be seen that the fouling layer formed at low pH is very resistant in the beginning and then breaks in big chunks, while the unadjusted pH seem to shear off continuously. The behaviour is similar for the two membranes.

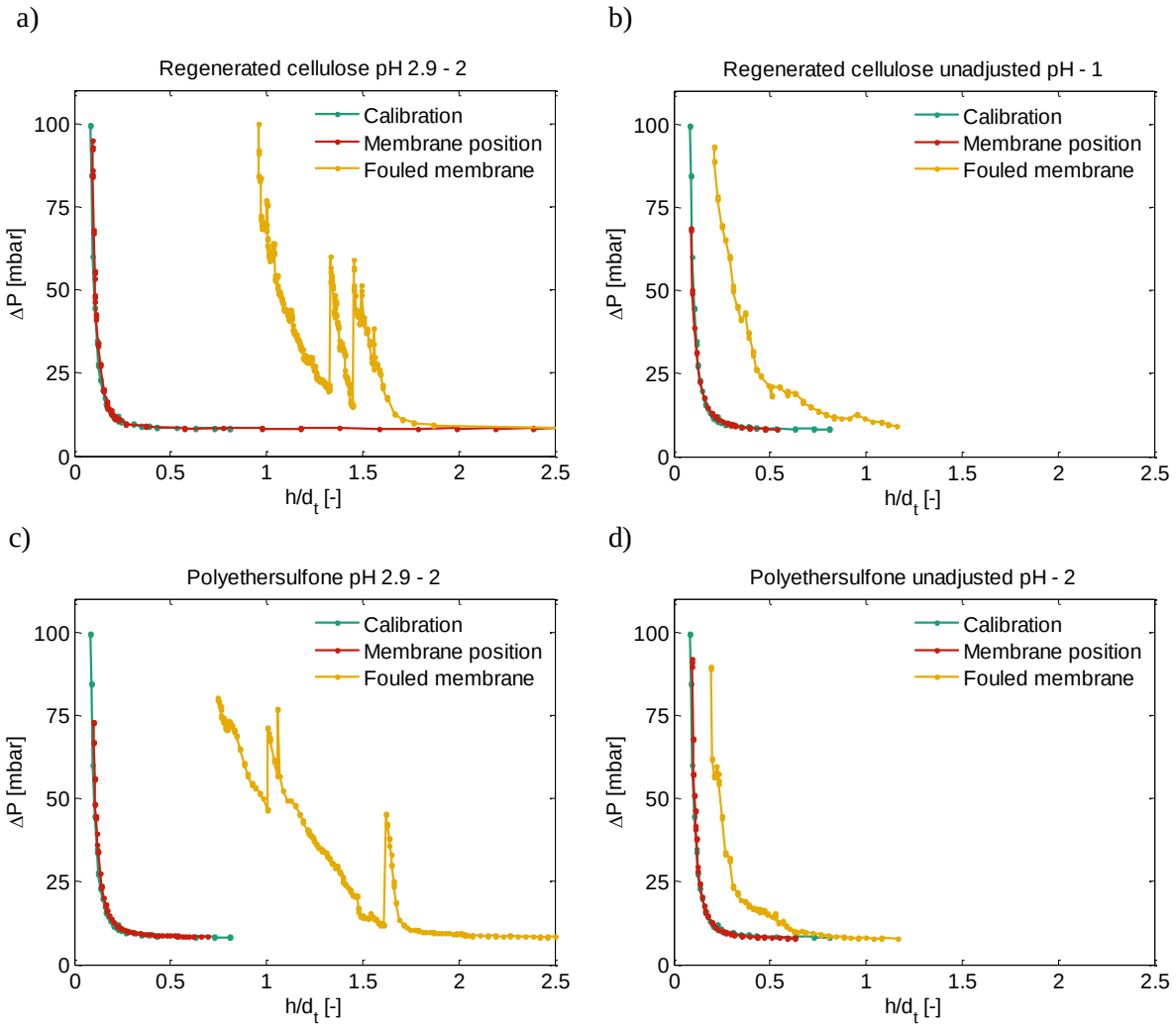

Figure 14. Plot of Δp vs h/d_t for the regenerated cellulose membrane. Showing the calibration curve (green) made with a solid plate, measurements made with the membrane after adjusting with $h_{0,offset}$ (red) and measurements on the fouling layer after adjusting with $h_{0,offset}$ (yellow). a) pH 2.9 regenerated cellulose membrane, b) unadjusted pH regenerated cellulose membrane, c) pH 2.9 polyethersulfone membrane, d) unadjusted pH polyethersulfone membrane.

In Fig. 15 the applied shear stress is plotted against the remaining thickness of the fouling layer, one plot for each membrane type. The flatter the pattern is, the more resistant the fouling layer is. Here it is also visible that acidic fouling layers are thicker and at least in the beginning they are more resistant. When some fouling layer chunks have been sheared off, they follow the same pattern as the ones with unadjusted pH. One replicate with the polyethersulfone membrane has a very resistant surface and no chunks are sheared off, only minor pieces.

The reason for the thicker and stronger fouling layers with low pH may be that the pores do not get blocked by the particles and that a higher flux is maintained for a longer time. Then a larger amount of the feed is transported to the membrane, which makes the fouling layer thicker. The particles that forms the fouling layer may then also be put under a higher compressible force than if most of the pressure is put on the particles that block the pores, which may be the situation in the cases with unadjusted pH. Further, at pH 2.9 the surface charges of both the membranes and the particles are around zero, so there are no repulsive forces that counteracts the build-up and compression of the fouling layer. The lack of repulsion, between particles and between the membrane and particles, may also lead to less structured

packing of the fouling layers, which could lead to an uneven distribution of the compressible forces. The more shear resistant parts may then have been put under large compressible forces and some regions in the fouling layers, which are less resistant to shear stress and suddenly shears off, may have been less compressed. The fouling layers at unadjusted pH, seems more evenly structured and shows much smaller variations in resistance, so the compression of those fouling layers seems more uniform.

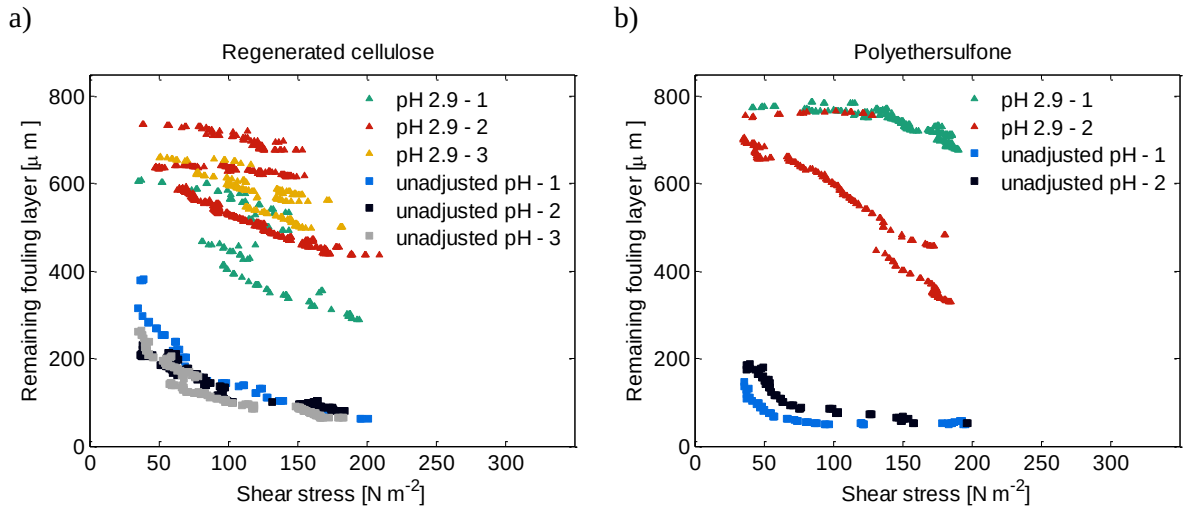

Figure 15. The shear stress applied at different height in the fouling layers. The triangles indicate pH 2.9 and the squares indicate unadjusted pH. a) Regenerated cellulose membrane, three replicates at each pH. b) Polyethersulfone membrane, two replicates at each pH.

Another noteworthy trend is that the fouling layers with unadjusted pH flattens out deeper down in the layers, at this point the thickness is about 50-80 µm. This corresponds to about 2.5 to 4.5 times the size of the average particle size in the cake, according to laser diffraction measurements presented in Section 4.3.1. The measurements may at this stage have been performed on single or multiple particles, with the orientation of each particle affecting the result. Therefore, it may be difficult to draw any definite conclusions regarding the adhesive strength of the fouling layer at this thickness.

All fouling layers can resist the same maximum shear stress, but at different heights in the layers. This is the maximum shear stress that can be applied and still get reliable results with the FDG equipment that was used.

4.3 Particle characterisation

4.3.1 Laser diffraction

Samples from the circulated feed suspension after filtration and suspended fouling layer was analysed using laser diffraction. The resulting size distributions for the samples from feed and fouling layer, are presented in Fig. 16. One representative sample from each pH level is presented here for clarity of figure, and all size distribution measurements can be found in Appendix IV. There were no obvious differences between the two membranes, so the size distributions in Fig. 16 are representative for both membranes.

a) b)

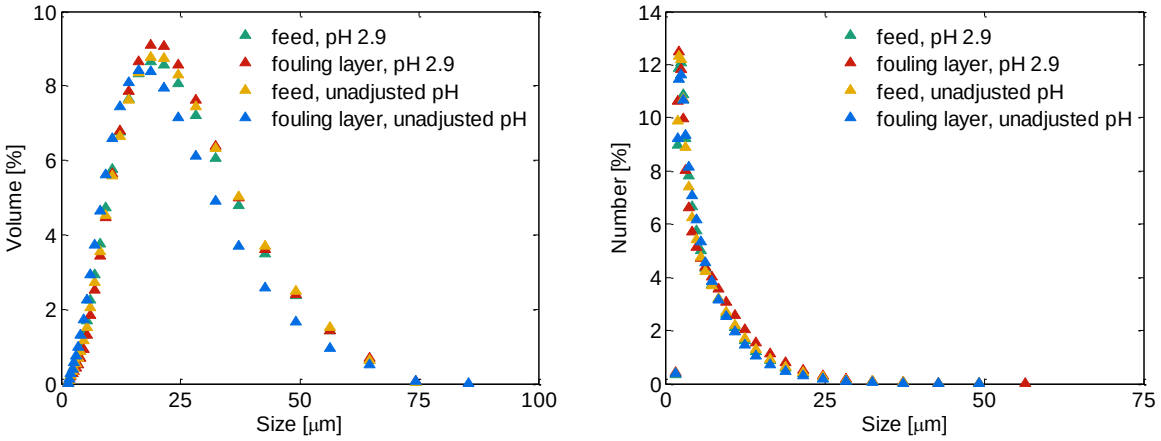

Figure 16. Particle size distribution from laser diffraction measurements for both pH levels and samples from the circulated feed suspension and from the fouling layer formed at the polyethersulfone membrane. a) Volume %, b) Number %

It can be seen that there are no large differences between the particle size distributions of for the two different pH levels, and there is thus no obvious indication of agglomeration at the low concentrations needed for this method. For both cases the smallest range where particles are detected is 1.4 - 1.7 µm, which indicates that no particles should have entered the pores (0.2 and 0.45 µm), and fouling only occurs on the surface of the membranes. The reason for the different shapes of the distributions for volume based (Fig. 16a) and number based (Fig. 16b) is that the large amount of small particles, in the number based chart, still take up a very small volume.

On the volume based distribution, there is a small difference between the fouling layer and feed for unadjusted pH, and the same small difference cannot be seen at pH 2.9. It indicates that it might be the smaller particles that mainly forms the fouling layer and more of the larger particles leaves with the retentate, for the unadjusted pH.

In Tab. 7 the average values of D_{10}, D_{50} and D_{90} are presented, where x% of the particles in the sample have a smaller diameter than the D_x-value. From the D-values it is also seen that there is a slight difference for the samples with unadjusted pH compared to the other samples, there are smaller particles in the fouling layer than in the feed suspension.

Table 7. Average D-values [µm] for the size distribution measurements performed with laser diffraction.

pH	sample	D_{10}	D_{50}	D_{90}
2.9	**feed**	7.4	18.2	38.1
	fouling	7.9	18.7	38.1
unadjusted	**feed**	7.4	18.4	38.7
	fouling	6.7	16.8	35.4

4.3.2 Focused beam reflectance measurements

Measurements with FBRM were performed at two different concentrations, 0.02 vol. % and 0.15 vol. %. The results from the latter is presented in Fig. 17 and the results from the lower concentration can be found in Appendix IV. The higher concentration gives more statistically reliable results, since it is based

on more particles. The concentration close to the membrane during filtration is most likely higher than in the feed flow, so the use of a higher concentration in these measurements may better represent the situation close to the membrane. The FBRM tests are only carried out once, which makes it hard to draw any firm conclusions from it, but it at least gives some indications of the differences between the pH levels.

From Fig. 17 it can be seen that there is no large difference in the chord length distribution for the different cases. It seems like the FBRM, like the laser diffraction measurements, there is no detection of any agglomerates in the low pH suspension. On the other hand, there is an obvious difference in the counts per second, hence the number of particles in the suspension, between the different cases. At low pH the counts per second decreases drastically. When increasing the stirring rate, the number of particles increases and decreasing the stirring rate again, the number of particles almost goes back to the same level before the increase in stirring rate. This might be an indication of sedimentation of particles at low pH. The sedimentation at low pH could be explained by formation of weak agglomerates at low pH. The agglomerates sediment to the bottom of the vessel when the shear stress from stirring is low. When shear stress is increased by higher stirring rate, those agglomerates break into their original individual particle structure. When the higher shear stress is removed, the particles agglomerates again.

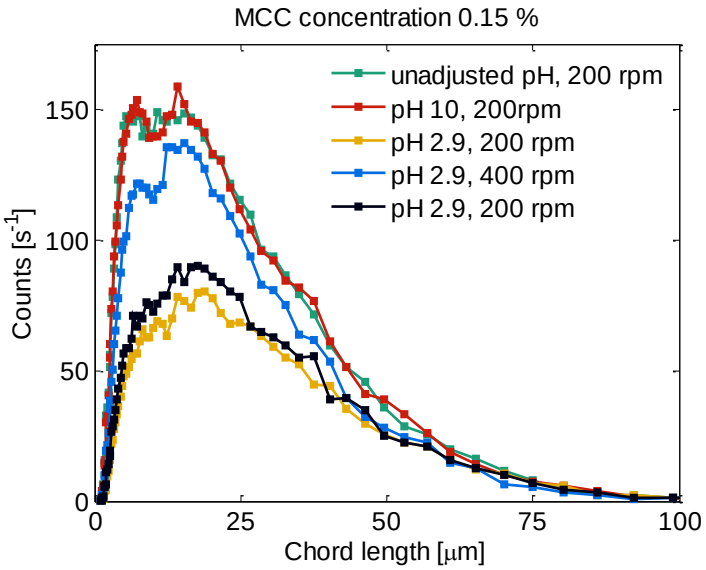

Figure 17. Chord length distribution from measurements with FBRM. The measurements were performed continuously, starting with unadjusted pH and 200 rpm stirring (green), followed by adding NaOH to pH 10 (red), then addition of H_2SO_4 to pH 2.9 (yellow). Then the stirring rate was increased to 400 rpm for a while (blue) and later decreased to 200 rpm again (black).

4.4 Sedimentation

Two sedimentation tests are presented in this section. One test with comparison between a suspension with adjusted pH and an unadjusted suspension, and one test with adjustment of ionic strength.

4.4.1 pH adjusted

The resulting photographs from the sedimentation tests are shown in Fig. 19. It is visible that the particles in the cylinder with pH adjusted to 2.9 settles faster than the particles in the unadjusted suspension, and after one hour no changes can be visually observed in this cylinder. In the cylinder with unadjusted pH, the suspension is more “milky”, also seen in Fig. 18b, and the particles settle slower. After ten minutes an indistinct boundary appears, between a clearer region on the top and a denser region below, the boundary goes down through the cylinder with time.

In the early stages of this experiments, larger particles could be visually observed in the cylinder with pH 2.9, Fig. 18a. It seems like the particles agglomerate into larger clusters and then settle faster than the single particles.

a) b)

Figure 18. Close ups of the bottom of the cylinders after 3 min of sedimentation. a) pH 2.9, b) unadjusted pH.

The particle size distribution in the middle of the cylinder with pH adjusted to 2.9, taken after 48h and 52h, could not be measured due to too low concentration of particles for the equipment to measure. In the cylinder with unadjusted pH, the particles were very small and the size distribution did not change considerably during the four hours between the samples. The size distribution is shown in Appendix V.

It should be mentioned that in these tests, the MCC concentration is 7.5 times higher than in the feed suspension used for filtration experiments. On the other hand, the concentration of particles close to the membrane in the filtration experiments should be considerably higher than in the feed suspension. A higher particle concentration implies that the particles can interact more, since they are closer to each other, and they can agglomerate and settle faster than for lower concentrations.

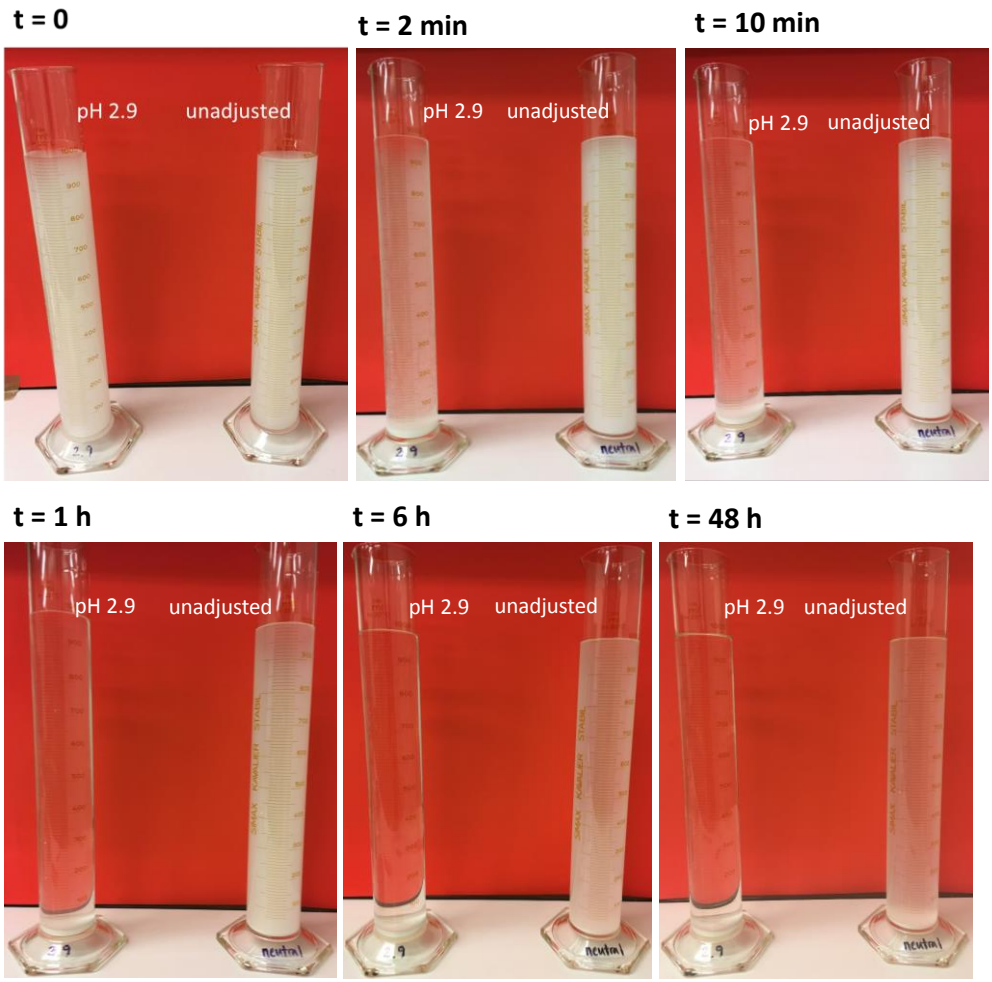

Figure 19. Photos of the cylinders for sedimentation tests with pH adjustment. In the cylinder to the left pH is adjusted to 2.9 by addition of sulfuric acid, and in the cylinder to the right pH is unadjusted. Time lapse from t= 0 to t= 48h. Photos from more time steps are shown in Appendix V.

4.4.2 Ionic strength adjusted

Photos from the sedimentation tests are shown in Fig. 20, with the cylinder with approximately the same ionic strength as the acidic one in Section 4.4.1 to the left and the cylinder with ten time higher ionic strength to the right.

After ten minutes, it can be seen that the particles in the cylinder the cylinder with ten times the ionic strength, settles faster than in the one with one time the ionic strength. After 24h, the cylinder with ten times the ionic strength is practically transparent and when performing particle size measurements after 25h, the particle concentration was too low to measure. The cylinder with one time the ionic strength is still fairly milky and the particle size measurements only show a small difference to the sample taken in the same cylinder four hours later. The particle size distribution is shown in Appendix V.

It is observed that sedimentation is faster when ions are added to shield the surface charge of the MCC particles, and when there are ten time more ions to shield the surface charges, the particles agglomerate easier and settle faster.

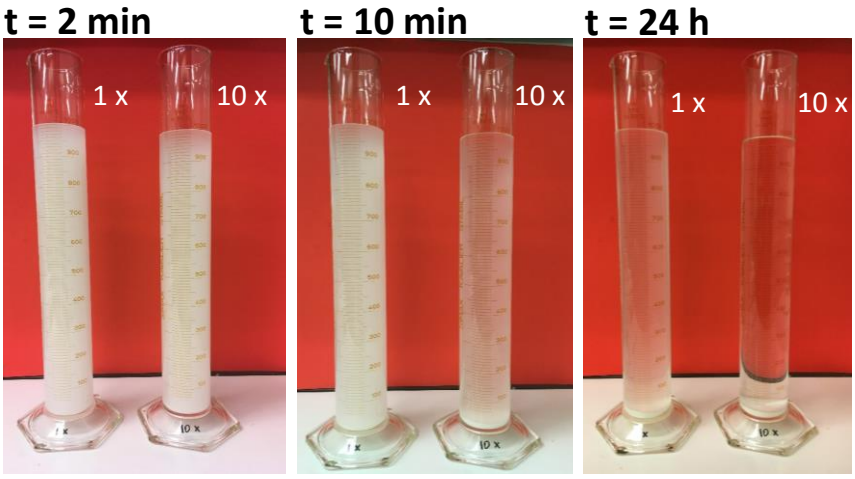

Figure 20. Photos of the cylinders for sedimentation tests with adjustment of ionic strength. In the cylinder to the left the ionic strength is adjusted the about same as for the one with pH 2.9 in Section 4.4.1, by addition of sodium sulphate, and in the cylinder to the right the ionic strength is ten times larger. Time lapse from t= 2min to t= 24h. Photos from more time steps are shown in Appendix V.

4.4.3 Comparison of the two sedimentation tests

From the photos for the both sedimentation test above, the highest sedimentation speed is observed in the cylinder with pH adjusted to 2.9. The second highest speed occurs in the cylinder with ten time the ionic strength, followed by the one with one time the ionic strength and finally, the slowest sedimentation occurs in the cylinder with unadjusted MCC suspension. It seems like sedimentation highly depends on the electrostatic interactions between particles, and that even ten times higher ionic strength do not manage to fully shield out the charges. This indicates that it is more efficient to eliminate the surface charges, by protonation of the carboxylic groups, than to shield the charges by addition of salt. But a larger amount of salt would probably give similar results as when adding acid.

The particle size distributions for the two slowest sedimentation tests are in the same size range, but they are taken after 48h for the unadjusted one and after 25h for the one with the low ionic strength.

The reason that the agglomeration was not visible in the particle size distributions, measured by laser diffraction, is most likely that then the measurements were performed at much lower particle concentration and with stirring. So, the particles could not interact as much as in the sedimentation experiments, and the stirring may have damaged the agglomerates that were eventually formed.

5 Conclusions

In this study, membrane filtration for the dewatering of microcrystalline cellulose was investigated with focus on the properties of the surface fouling layers at different operational pH, representing different electrostatic interactions between particles and between the membrane and particles.

From measurements with fluid dynamic gauging, it was found that there is an obvious difference in the fouling behaviour for a suspension with pH 2.9 compared to a suspension with unadjusted pH. Thicker and stronger surface fouling layers were formed at pH 2.9. No large differences were observed between the two investigated membranes.

The rapid permeate flux decline for the MCC suspension with unadjusted pH indicates pore blocking. For this case, the pressure drop would be mainly due to the particles that block the pores and the low flux brings fewer particles to the fouling layer. This most likely gives the formation of thin fouling layers with low resistance to fluid shear stress, which was observed by FDG measurements. The electrostatic interactions, with repulsion between particles and between particles and the membrane, could also decrease the cohesive strength and the thickness of the fouling layer.

The flux decline for the MCC suspensions with pH 2.9 was not as distinct, which may indicate that there is less pore blocking under these conditions. The higher flux brings more particles into the surface fouling layer, and the pressure drop is over all the particles in the fouling layer, giving higher compressible forces on the fouling layer. Furthermore, the repulsive forces, between particles and between particles and the membrane, are neutralised at pH 2.9. Together, this contributes toward thicker fouling layers that are more resistant to the fluid shear stress, which were observed by the FDG measurements.

At pH 2.9, when the surface charges of the particles are neutralised, the MCC particles agglomerates and this causes faster sedimentation than at unadjusted pH, which would also contribute to the thicker fouling layers at pH 2.9. The shielding effect from ions also gives agglomeration and faster sedimentation, but the effect is not as large as when the charges are neutralised.

6 Future work

In this study, the surface charge of the MCC particles were both neutralised and shielded by ions in the low pH suspensions. One simple sedimentation experiment was carried out with the addition of salt instead of acid, and thus only with shielding of the surface charges. To further compare the effect of shielding with the experiments in this study, FDG measurements could also be performed with salt addition instead of acid.

The sedimentation tests performed in this study were simple, better experiments with use of standard sedimentation equipment would lead to more quantitative conclusions on the sedimentation velocity. It would also be interesting to test the particle size distribution in the sediment.

A measure of the cohesive forces between particles and between the membrane and particles at particle level, would be helpful to understand the results from this study better. To do this, atomic force microscopy could be used on the fouling layers formed at the different pH levels.

To understand the flow patterns close to the membrane, CFD simulations could be performed. This would give a better view of the local concentration and the settling of MCC on the membrane, as well as the interaction between particles. Since it is a complex system, with both particles and a membrane, these simulations would however be very difficult to perform.

The verify which fouling phenomena that is present for the two pH levels, critical flux analysis could be performed as described in Section 2.1.5. This would give the critical flux and the transition flux between two fouling phenomena.

7 Nomenclature

Roman

A_m	Membrane area	m^2
c_1,c_2,c_3,c_4	Constants used in regression fit	-
c_b	Particle concentration in feed bulk	kg m^{-3}
c_{bp}	Mass of solids per unit permeate volume	kg m^{-3}
C_d	Discharge coefficient	-
c_m	Concentration at membrane surface	kg m^{-3}
c_p	Particle concentration in permeate	kg m^{-3}
d	FDG gauge tube diameter	m
d_t	Nozzle diameter	m
h	Height over fouling layer	m
h_0	Height over membrane surface	m
$h_{0,offset}$	Calibration offset value	m
J	Permeate flux	m s^{-1}
J^*	Critical flux	m s^{-1}
J_0	Initial permeate flux	m s^{-1}
k	Coefficient in fouling models	varies
l_{eff}	Effective length	m
m_g	Gauging mass flow rate	kg s^{-1}
n	Index in fouling models	-
P	Pressure	Pa
P_a	Parameter	Pa
P_{feed}	Feed pressure	Pa
P_{perm}	Permeate pressure	Pa
P_{ret}	Retentate pressure	Pa
P_s	Local solid compressive pressure	Pa
R	Retention	m^{-1}
R_c	Cake resistance	m^{-1}
R_{cp}	Concentration polarization resistance	m^{-1}
R_m	Membrane resistance	m^{-1}
R_p	Pore fouling resistance	m^{-1}
t	Time	s
TMP	Transmembrane pressure	Pa
TMP_{avg}	Average transmembrane pressure	Pa
V	Permeate volume	m^3
V_{solid}	Volume of solids	m^3
V_{total}	Total volume	m^3

Greek

Δp	Pressure difference	Pa
μ	Viscosity	Pa s
K	Cake permeability	m^2
K_m	Membrane permeability	m^2

α_0	Parameter	m kg^{-1}
α_c	Specific cake filtration resistance	m kg^{-1}
β	Parameter	-
δ	Fouling layer thickness	m
δ_m	Membrane thickness	m
ε	Porosity	-
Π	Osmotic pressure	Pa
ρ_L	Density of liquid	kg m^{-3}
ρ_s	Density of solids	kg m^{-3}
σ	Blocked area per unit permeate volume	m^{-1}
τ_w	Shear stress	Pa
$\tau_{w,max}$	Maximal shear stress	Pa
ϕ	Solidosity	-
ϕ_0	Parameter	-
ϕ_{ads}	Adsorbed particle volume fraction	-

Acronyms

CFV	Cross-flow velocity
DI	Deionized
FBRM	Focused beam reflectance measurement
FDG	Fluid dynamic gauging
LVDT	Linear variable differential transformer
MCC	Microcrystalline cellulose
MF	Microfiltration
MWCO	Molecular weight cut-off
NF	Nanofiltration
pDADMAC	Polydiallyldimethylammonium chloride
RO	Reverse osmosis
UF	Ultrafiltration

8 References

ABOABBOUD, M. & ELMASALLATI, S. 2007. Potable water production from seawater by the reverse osmosis technique in Libya. *Desalination,* 203**,** 119-133.

AHMAD, S. & AHMED, S. M. 2014. Application of membrane technology in food processing. *Food Processing: Strategies for Quality Assessment.* Springer.

ALTENA, F. W. & BELFORT, G. 1984. Lateral migration of spherical particles in porous flow channels: application to membrane filtration. *Chemical Engineering Science,* 39**,** 343-355.

BELFORT, G., DAVIS, R. H. & ZYDNEY, A. L. 1994. The behavior of suspensions and macromolecular solutions in crossflow microfiltration. *Journal of Membrane Science,* 96**,** 1-58.

BERK, Z. 2013. *Food Process Engineering and Technology,* San Diego, UNITED STATES, Elsevier Science & Technology.

BOLTON, G., LACASSE, D. & KURIYEL, R. 2006. Combined models of membrane fouling: Development and application to microfiltration and ultrafiltration of biological fluids. *Journal of Membrane Science,* 277**,** 75-84.

BRUGGEN, B. V. D., VANDECASTEELE, C., GESTEL, T. V., DOYEN, W. & LEYSEN, R. 2003. A review of pressure‐driven membrane processes in wastewater treatment and drinking water production. *Environmental Progress,* 22**,** 46-56.

CARDEW, P. T. & LE, M. S. 1998. Chapter 2 Membrane Technologies. *Membrane Processes: A Technology Guide*. The Royal Society of Chemistry.

CHEW, J. Y. M., CARDOSO, S. S. S., PATERSON, W. R. & WILSON, D. I. 2004a. CFD studies of dynamic gauging. *Chemical Engineering Science,* 59**,** 3381-3398.

CHEW, J. Y. M., PATERSON, W. R. & WILSON, D. I. 2004b. Fluid dynamic gauging for measuring the strength of soft deposits. *Journal of Food Engineering,* 65**,** 175-187.

CHEW, J. Y. M., PATERSON, W. R., WILSON, D. I., HÖUFLING, V. & AUGUSTIN, W. 2005. A Method for Measuring the Strength of Scale Deposits on Heat Transfer Surfaces. *Developments in Chemical Engineering and Mineral Processing,* 13**,** 21-30.

DARCY, H. 1856. *Les fontaines publiques de la ville de Dijon: exposition et application,* Victor Dalmont.

ECKSTEIN, E. C., BAILEY, D. G. & SHAPIRO, A. H. 2006. Self-diffusion of particles in shear flow of a suspension. *Journal of Fluid Mechanics,* 79**,** 191-208.

FIELD, R. 2010. Fundamentals of fouling. *Membranes for water treatment,* 4**,** 1-23.

FIELD, R. W., WU, D., HOWELL, J. A. & GUPTA, B. B. 1995. Critical flux concept for microfiltration fouling. *Journal of Membrane Science,* 100**,** 259-272.

FRYER, P. J., SLATER, N. K. H. & DUDDRIDGE, J. E. 1985. Suggestions for the operation of radial flow cells in cell adhesion and biofouling studies. *Biotechnology and Bioengineering,* 27**,** 434-438.

GREEN, D. W., PERRY, R. H. & DAWSONERA 2008. *Perry's chemical engineers' handbook,* London;New York;, McGraw-Hill.

GU, T., ALBERT, F., AUGUSTIN, W., CHEW, Y. M. J., MAYER, M., PATERSON, W. R., SCHOLL, S., SHEIKH, I., WANG, K. & WILSON, D. I. 2011. Application of fluid dynamic gauging to annular test apparatuses for studying fouling and cleaning. *Experimental Thermal and Fluid Science,* 35**,** 509-520.

GU, T., CHEW, Y. M. J., PATERSON, W. R. & WILSON, D. I. 2009. Experimental and CFD studies of fluid dynamic gauging in duct flows. *Chemical Engineering Science,* 64**,** 219-227.

HENLEY, E. J., SEADER, J. D. & ROPER, D. K. 2011. *Separation process principles,* Hoboken, N.J, Wiley.

HERMANS, P. 1936. Principles of the mathematical treatment of constant-pressure filtration. *J. Soc. Chem. Ind.,* 55**,** 1-4.

HERMIA, J. 1982. Constant pressure blocking filtration laws - application to power-law non-Newtonian fluids. . *Trans. IChemE. ,* 60**,** 183-187.

JACKSON, G. F. 1978. An assessment of the application of pneumatic gauging to the measurement of mass transfer coefficients. *Journal of Physics E: Scientific Instruments,* 11**,** 569.
JONES, S. A., CHEW, Y. M. J., BIRD, M. R. & WILSON, D. I. 2010. The application of fluid dynamic gauging in the investigation of synthetic membrane fouling phenomena. *Food and Bioproducts Processing,* 88**,** 409-418.
LEWIS, W. 2014. Advanced Studies of Membrane Fouling: Investigation of Cake Fouling Using Fluid Dynamic Gauging. *In:* UNIVERSITY OF BATH, D. O. C. E. (ed.). Bath.
LEWIS, W. J. T. 2015. FDG Stepper System User's Manual and Reference Guide. Bath: University of Bath, Department of Chemical Engineering.
LEWIS, W. J. T., AGG, A., CLARKE, A., MATTSSON, T., CHEW, Y. M. J. & BIRD, M. R. 2016. Development of an automated, advanced fluid dynamic gauge for cake fouling studies in cross-flow filtrations. *Sensors and Actuators A: Physical,* 238**,** 282-296.
LEWIS, W. J. T., CHEW, Y. M. J. & BIRD, M. R. 2012. The application of fluid dynamic gauging in characterising cake deposition during the cross-flow microfiltration of a yeast suspension. *Journal of Membrane Science,* 405-406**,** 113-122.
LEWIS, W. J. T., MATTSSON, T., CHEW, Y. M. J. & BIRD, M. R. 2017. Investigation of cake fouling and pore blocking phenomena using fluid dynamic gauging and critical flux models. *Journal of Membrane Science,* 533**,** 38-47.
LI, H., FANE, A. G., COSTER, H. G. L. & VIGNESWARAN, S. 1998. Direct observation of particle deposition on the membrane surface during crossflow microfiltration. *Journal of Membrane Science,* 149**,** 83-97.
LI, H., FANE, A. G., COSTER, H. G. L. & VIGNESWARAN, S. 2000. An assessment of depolarisation models of crossflow microfiltration by direct observation through the membrane. *Journal of Membrane Science,* 172**,** 135-147.
MAIRAL, A. P., GREENBERG, A. R., KRANTZ, W. B. & BOND, L. J. 1999. Real-time measurement of inorganic fouling of RO desalination membranes using ultrasonic time-domain reflectometry. *Journal of Membrane Science,* 159**,** 185-196.
MATTSSON, T., LEWIS, W. J. T., CHEW, Y. M. J. & BIRD, M. R. 2017. The use of fluid dynamic gauging in investigating the thickness and cohesive strength of cake fouling layers formed during cross-flow microfiltration. *Separation and Purification Technology*.
MATTSSON, T., SEDIN, M. & THELIANDER, H. 2012. Filtration properties and skin formation of micro-crystalline cellulose. *Separation and Purification Technology,* 96**,** 139-146.
MULDER, M., SPRINGERLINK, A. & SPRINGERLINK 1991. *Basic Principles of Membrane Technology,* Dordrecht, Springer Netherlands.
PHILLIPS, G. O. & WILLIAMS, P. A. 2009. Microcrystalline cellulose. *Handbook of Hydrocolloids (2nd Edition).* Cambridge: Woodhead Publishing.
SALLEY, B., GORDON, P. W., MCCORMICK, A. J., FISHER, A. C. & WILSON, D. I. 2012. Characterising the structure of photosynthetic biofilms using fluid dynamic gauging. *Biofouling,* 28**,** 159-173.
SCHLUEP, T. & WIDMER, F. 1996. Initial transient effects during cross flow microfiltration of yeast suspensions. *Journal of Membrane Science,* 115**,** 133-145.
SHIRATO, M., SAMBUICHI, M., KATO, H. & ARAGAKI, T. 1969. Internal flow mechanism in filter cakes. *AIChE Journal,* 15**,** 405-409.
STRATHMANN, H. 2011a. Membrane Separation Processes, 1. Principles.
STRATHMANN, H. 2011b. Membrane Separation Processes, 4. Concentration Polarization and Membrane Fouling.
THUVANDER, J., ARKELL, A. & JÖNSSON, A. S. 2014. Centrifugation as pretreatment before ultrafiltration of hemicelluloses extracted from wheat bran. *Separation and Purification Technology,* 138**,** 1-6.
TILLER, F. M. & GREEN, T. C. 1973. Role of porosity in filtration IX skin effect with highly compressible materials. *AIChE Journal,* 19**,** 1266-1269.
TILLER, F. M. & LEU, W.-F. 1980. BASIC DATA FITTING IN FILTRATION. *J CHIN INST CHEM ENG,* V 11**,** 61-70.

TULADHAR, T. R., PATERSON, W. R., MACLEOD, N. & WILSON, D. I. 2000. Development of a novel non-contact proximity gauge for thickness measurement of soft deposits and its application in fouling studies. *Canadian Journal of Chemical Engineering,* 78**,** 935-947.

WETTERLING, J., MATTSSON, T. & THELIANDER, H. 2017. Local filtration properties of microcrystalline cellulose: Influence of an electric field. *Chemical Engineering Science,* 171**,** 368-378.

ZHOU, M. & MATTSSON, T. 2018. Cohesive strength of membrane surface fouling layers - effect of crossflow regimes. *In:* F. LIPNIZKI, D. I. W., Y.M.J. CHEW, A.-S. JÖNSSON (ed.) *Fouling and Cleaning in Food Processing.* Lund: Department of Chemical Engineering, Lund University

Appendix I

The surface weight was calculated as follows in Eqs. I-V.

$$V_{recovery} = \frac{m_{H_2O,recovery}}{\rho_{H_2O}} \quad \text{(I)}$$

$$m_{MCC,recovery} = V_{recovery} \cdot c_{MCC} \cdot \rho_{MCC} \quad \text{(II)}$$

$$m_{MCC} = m_{MCC+beaker} - m_{beaker} - m_{MCC,recovery} \quad \text{(III)}$$

$$A_{membrane} = \frac{l_{membrane,1} + l_{membrane,2}}{2} \cdot w_{membrane} \quad \text{(IV)}$$

$$surface\ weight = \frac{m_{MCC}}{A_{membrane}} \quad \text{(V)}$$

Where $V_{recovery}$ is the volume of the liquid that is pushed out by injecting air while recovering the cake, $m_{H2O,\ recovery}$ is the mass of this liquid and ρ_{H2O} is the density of water. $m_{MCC,\ recovery}$ is the amount of MCC in the recovery liquid, c_{MCC} is the concentration of MCC particles in the feed and ρ_{MCC} is the density of MCC. m_{MCC} is the mass of MCC in the part of the fouling layer that is used for the calculations, m_{beaker} is the mass of the beaker that the fouling is collected in, $A_{membrane}$ is the surface area of the part of membrane that is used for the calculations, $l_{membrane,\ i}$ is the length of each side of the membrane if the membrane was unevenly cut, and $w_{membrane}$ is the width of the membrane.

Appendix II

The flux profiles from the experiments performed to measure the surface weight of the fouling layers are presented in Fig. I.

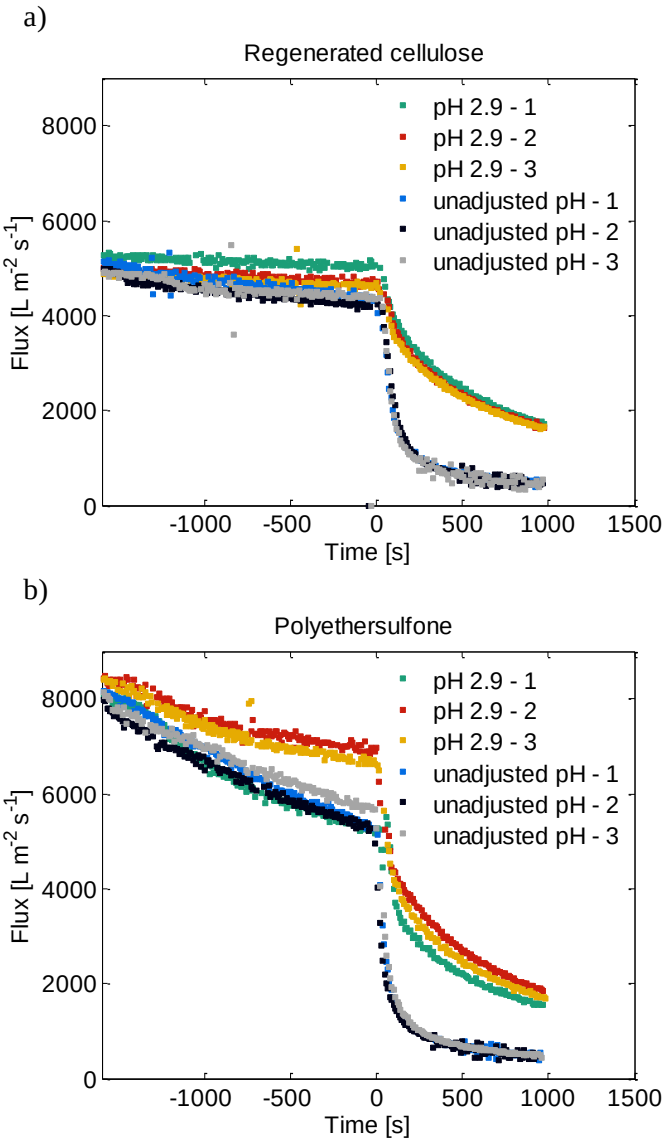

Figure I. Flux profiles for the experiments for surface weight calculations. The time axis is adjusted to be zero at the time for addition of MCC to the feed. a) Regenerated cellulose membrane, three replicates at each pH. b) Polyethersulfone membrane, three replicates at each pH.

Appendix III

Figure II shows the FDG plots that are not included in the main report.

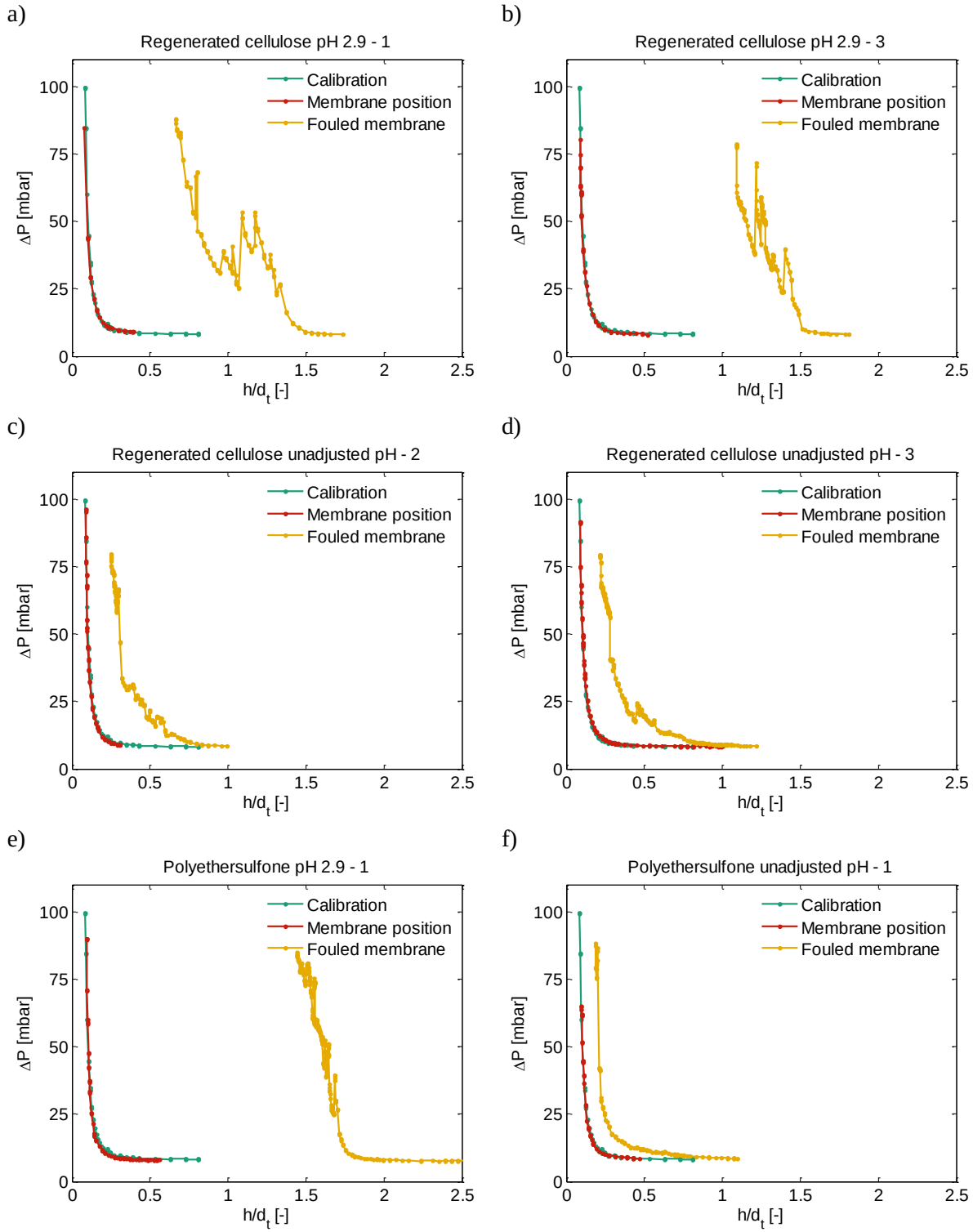

Figure II. Plot of Δp vs h/d_t for the regenerated cellulose membrane. Showing the calibration curve (green) made with a solid plate, measurements made with the membrane after adjusting with $h_{0,offset}$ (red) and measurements on the fouling layer after adjusting with $h_{0,offset}$ (yellow). a) pH 2.9 regenerated cellulose membrane, replicate 1, b) pH 2.9 regenerated cellulose membrane, replicate 3, c) unadjusted pH regenerated cellulose membrane, replicate 2 d) unadjusted pH regenerated cellulose membrane, replicate 3, e) pH 2.9 polyethersulfone membrane, replicate 1 f) unadjusted pH polyethersulfone membrane, replicate 1.

Appendix IV

In Fig. III the particle size distributions from laser diffraction is presented, and in Fig. IV the FBRM measurements with MCC concentration of 0.02 % are shown.

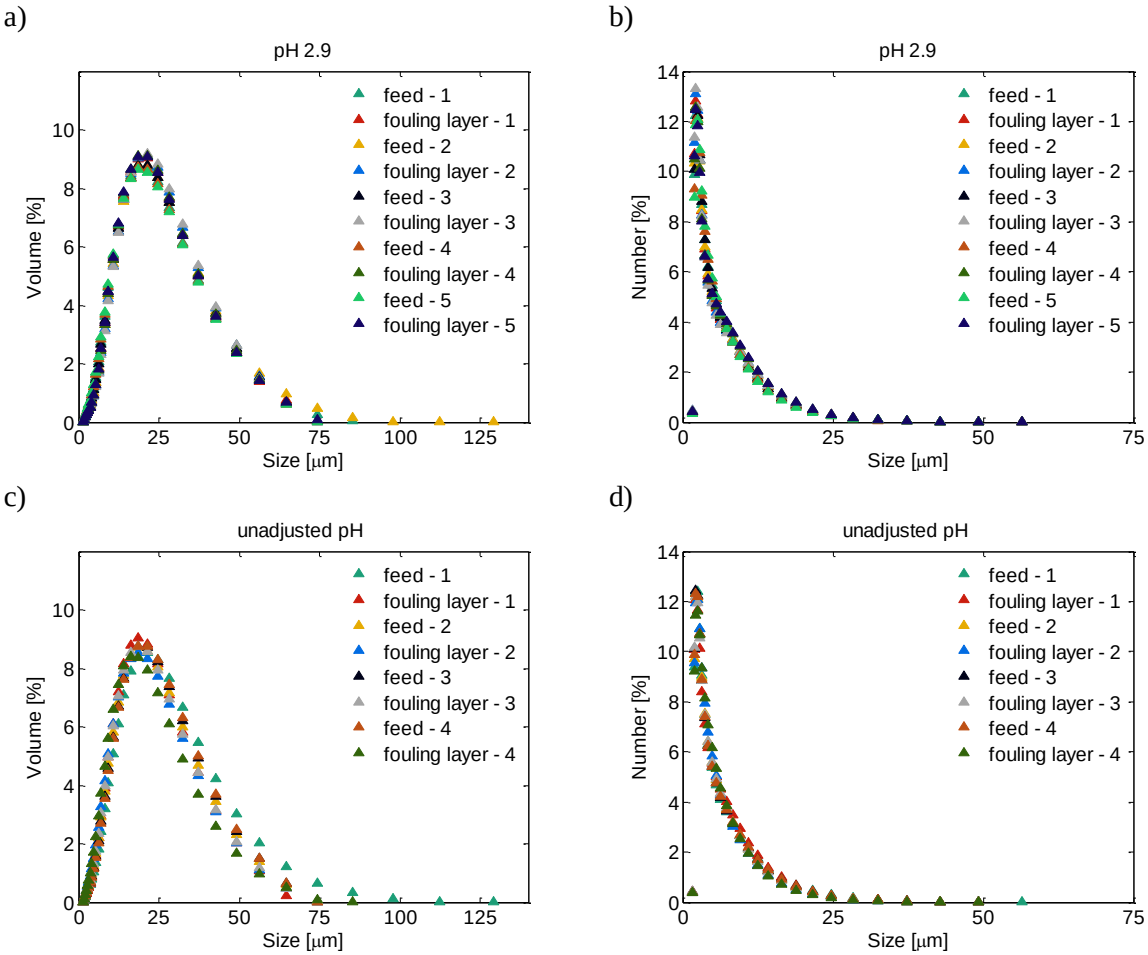

Figure III. Particle size distributions from laser diffraction measurements on the feed suspension and the fouling layer for the different pH levels. a) pH 2.9, volume based distribution, b) pH 2.9, number based distribution, c) unadjusted pH, volume based distribution, d) unadjusted pH, number based distribution

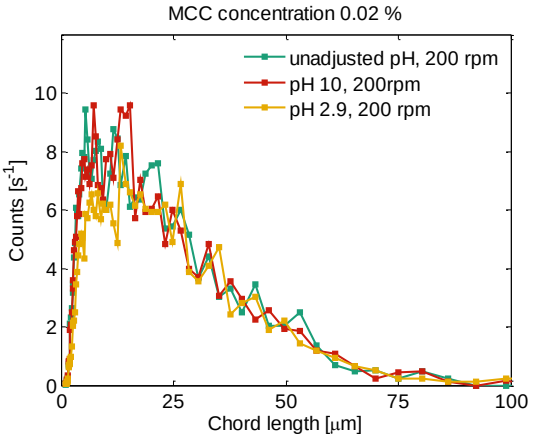

Figure IV. Chord length distribution from measurements with FBRM with MCC concentration of 0.02%. The measurements were performed continuously, starting with unadjusted pH and 200 rpm stirring (green), followed by adding NaOH to pH 10 (red), then addition of H_2SO_4 to pH 2.9 (yellow).

Appendix V

In Fig. V, photos from the sedimentation test with adjustment of pH of the MCC suspensions are shown.

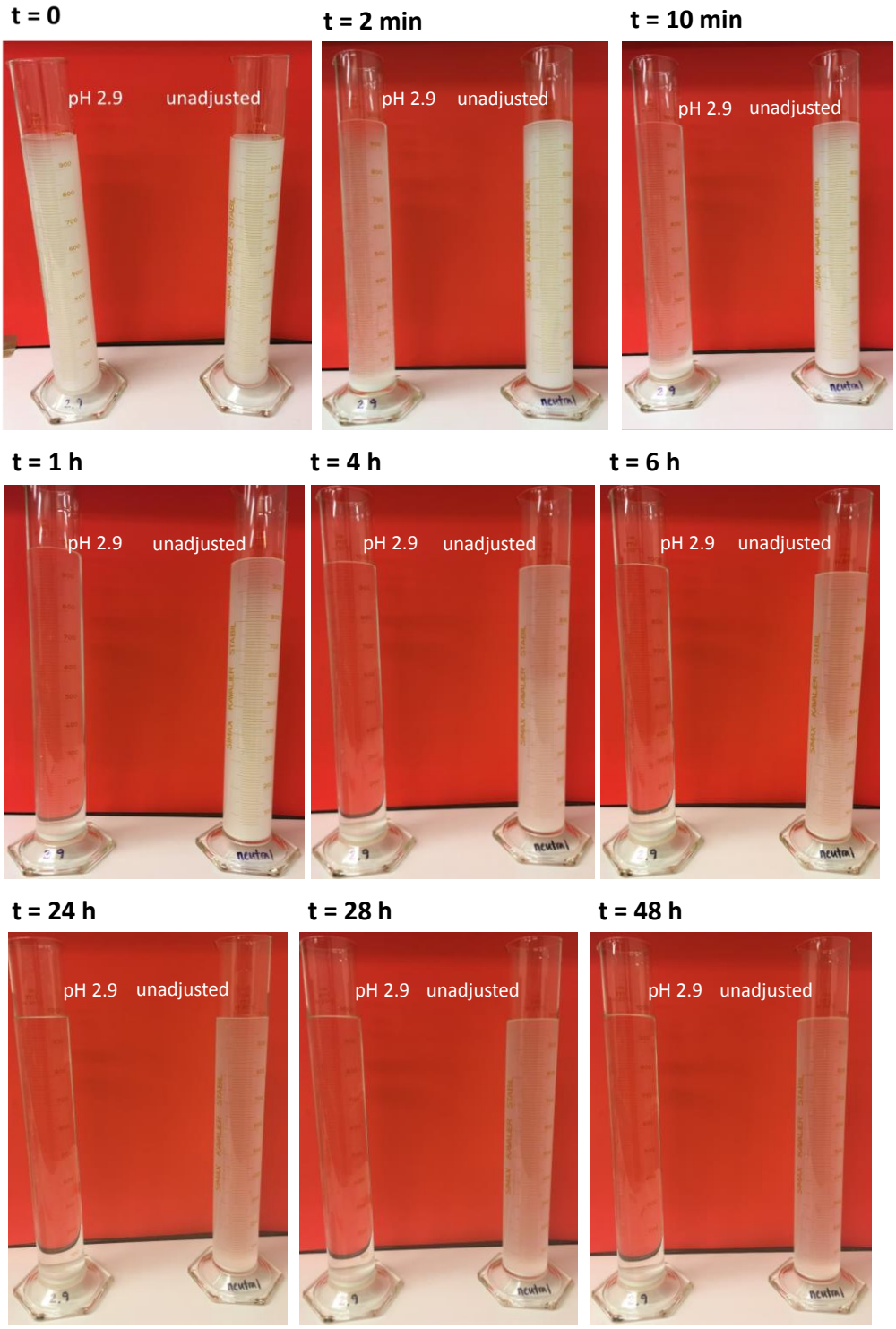

Figure V. Photos of the cylinders for sedimentation tests with pH adjustment. In the cylinder to the left pH is adjusted to 2.9 by addition of sulfuric acid, and in the cylinder to the right pH is unadjusted. Time lapse from t= 0 to t= 48h.

In Fig. VI, photos from the sedimentation test with adjustment of ionic strength of the MCC suspensions are shown.

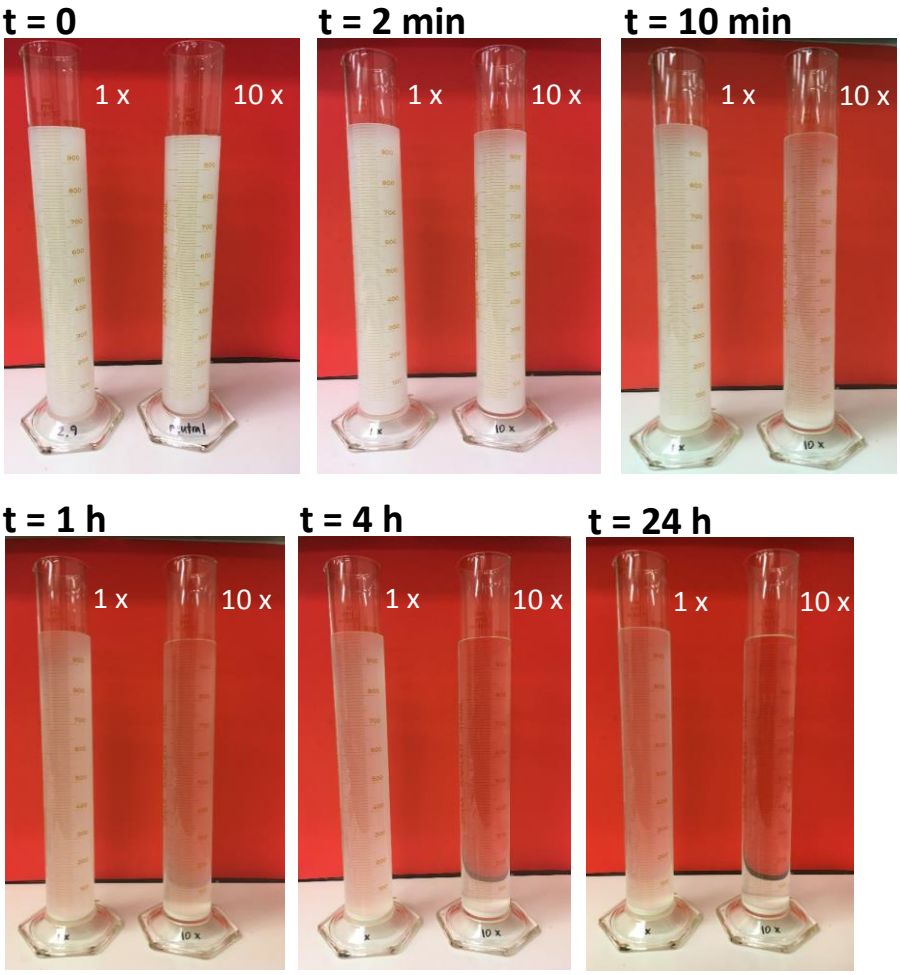

Figure VI. Photos of the cylinders for sedimentation tests with adjustment of ionic strength. In the cylinder to the left the ionic strength is adjusted the about same as for the one with pH 2.9 in Section 4.4.1, by addition of sodium sulphate, and in the cylinder to the right the ionic strength is ten times larger. Time lapse from t= 0 to t= 24h.

In Fig. VII, the particle size distributions made in the end of the sedimentation tests are shown.

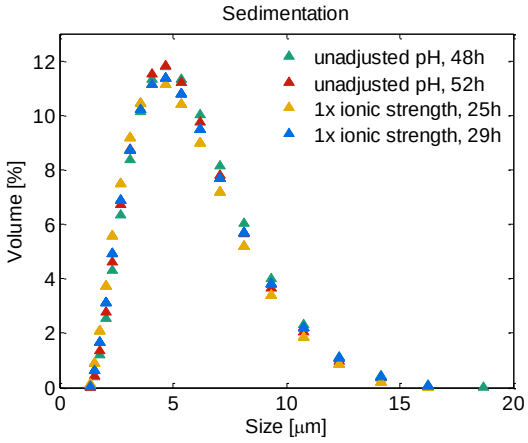

Figure VII. Particle size distribution by laser diffraction on samples taken in the middle of the cylinders in the end of the sedimentation tests.